Understanding NO_2 Sensing Mechanism on CdS Quantum Dots *via* Experimental and First-Principles Calculations

Krushna R. Zoting[1], Laxman N. Bhoye[2], Ankit Kumar[3], Om G. Jadhav[4], Vamshi Krishna Sabbi[4], Balaji G. Ghule[5], Haribhau M. Gholap*[1]*

[1]Department of Physics, Fergusson College (Autonomous), Savitribai Phule Pune University Pune,411004, MS, INDIA

[2]Department of Physics, SNJB's K.K.H.A. Arts, S.M.G.L Commerce and S.P.H.J, Science College Chandwad, Nashik-422003, MS, India, Affiliated to Savitribai Phule Pune University, Pune, MS, INDIA

[3]Department of Physics, Indian Institute of Science Education and Research, Dr. Homi Bhabha road, Panchawati, Pune-411018, MS, INDIA

[4]High-Performance Computing (HPC) Technologies Group, Center for Development of Advance Computing(C-DAC), Pune - 411008, MS, INDIA

[5]School of Chemistry, University College Cork, Cork-T12YT20, Republic of Ireland.

Corresponding authors: Balaji G. Ghule, bghule@ucc.ie **Haribhau M. Gholap,** haribhau.gholap@fergusson.edu

Abstract: - Nitrogen dioxide (NO_2) is a highly toxic atmospheric pollutant, necessitating sensing materials that combine high efficiency, selectivity, and rapid response. In this work, cadmium sulfide (CdS) quantum dots (QDs) were synthesized *via* a wet-chemical precipitation route and extensively characterized using XRD, Raman, UV-Vis absorption, PL/TRPL, XPS, FESEM–EDX, BET–BJH, and HRTEM. The QDs crystallize in the cubic phase with a particle size of 4–5 nm, exhibiting strong quantum confinement and high surface activity. Time-resolved PL measurements revealed a long decay lifetime of 7.11 μs, indicative of effective trap-assisted charge retention that favors gas sensing. Experimentally, the CdS QD sensor delivered a notable NO_2 response of 78% at 125 °C (at 40 ppm), with fast response and recovery times of 6 s and 24 s, along with excellent selectivity and operational stability. Density functional theory (DFT) calculations using the $GGA + U$ method showed that adsorption is strongly site-dependent: NO_2 binds most strongly at the S site (E_{ads} = –0.88 eV, charge transfer = +2.595 e), while N-on-Cd exhibits weak physisorption (–0.14 eV, +0.040 e). Optical conductivity derived from $\varepsilon_2(\omega)$ indicated enhanced $\sigma(\omega)$ for Cd-site adsorption, supporting rapid activation, whereas S-site chemisorption governs sensitivity. These synergistic effects highlight CdS QDs as promising candidates for high-performance NO_2 sensing.

Keywords - Cadmium sulfide quantum dots, Nitrogen dioxide sensing, Charge transfer dynamics, Density functional theory, Gas adsorption mechanism, optoelectronic properties.

1. Introduction

The combustion of fossil fuels, various industrial processes, and vehicle exhaust are the main sources of nitrogen dioxide (NO_2), a highly toxic atmospheric pollutant. NO_2 causes respiratory conditions and environmental deterioration even at trace levels by producing acid rain and photochemical smog. [1-2]. Therefore, accurate and real-time NO_2 monitoring is crucial for public health and environmental safety. [3]. To achieve accurate NO_2 detection, a variety of sensing technologies have been investigated, such as electrochemical, optical, and metal oxide semiconductor (MOS)-based systems. Among these, MOS sensors based on ZnO, SnO_2, WO_3, and In_2O_3 have shown exceptional chemical stability and sensitivity [4-5]; however, their high operating temperatures (>200 °C) lead to increased energy consumption, limited long-term stability, and device degradation [3,6]. While optical sensors are precise but require complicated instrumentation, making them unsuitable for portable or low-cost applications, electrochemical sensors are small and inexpensive but have short operational lifetimes and cross-sensitivity [7]. To overcome these limitations, two-dimensional (2D) materials like MoS_2, WS_2, and graphene oxide have been proposed. Their high surface area and adjustable band structures make them attractive. However, their practical use is limited by problems with reproducibility and environmental instability. Conducting polymers, like polyaniline and polypyrrole, are flexible and can work at room temperature. However, they have poor selectivity and are easily damaged by humidity [8-10].

In recent years, QDs have emerged as a new frontier in gas-sensing materials, bridging these requirements through their unique physicochemical characteristics [11]. CdS QDs have attracted a lot of attention among these materials due to their tunable bandgap, high surface-to-volume ratio, and strong surface reactivity, all of which are caused by quantum confinement effects. [12]. These properties not only enhance the adsorption of gas molecules but also facilitate quick and efficient charge transfer between the gas and the semiconductor surface [13]. In n-type semiconductors such as CdS, exposure to oxidizing gases like NO_2 typically results in electron withdrawal from the conduction band, causing a measurable increase in resistance [13]. The nature of this modulation is significantly influenced by surface states, the arrangement of defects, and the strength of

interactions between the gas and the surface. Therefore, a detailed comprehension of these charge-transfer processes at the atomic level is essential for enhancing sensitivity, selectivity, response time and stability [13]. The creation and characterization of CdS-based nanostructures for gas sensing have improved substantially, however there is still a lack of microscopic knowledge regarding charge redistribution, adsorption energetics, and electronic structure modification after NO_2 exposure [14]. Previous investigation has mostly concentrated on macroscopic response behavior without clarifying the underlying electrical interactions that cause sensitivity enhancement. To address this gap, the current work combines first-principles DFT calculations with experimental NO_2 sensing analysis to understand the charge transfer kinetics at the CdS–NO_2 interface. By providing atomic-scale insights into adsorption mechanisms and interfacial electronic interactions, this combined experimental–theoretical approach establishes a mechanistic understanding that permits the conceptual design of CdS-based QD systems for highly effective and stable NO_2 detection under ambient conditions.

2. Materials and Methods

2.1 Materials

All reagents used in the present study was analytical grade and required no further purification. Sigma-Aldrich supplies the sodium sulfide ($Na_2S{\cdot}9H_2O$, ≥98%), thioglycolic acid (TGA, ≥99%), and cadmium chloride ($CdCl_2$, ≥99%). Ethanol (99.9%, Merck) was used for dispersion and washing. For all solution preparations, deionized (DI) water with a resistivity of 18.2 MΩ·cm was used.

2.2 Synthesis of CdS QDs:

CdS QDs were synthesized using a wet chemical precipitation method, as illustrated in Scheme 1 [15]. Briefly, 2 mM $CdCl_2$ was dissolved in 100 mL of deionized (DI) water under constant magnetic stirring, followed by the dropwise addition of 18 mM thioglycolic acid (TGA), serving as a stabilizing and capping agent. After 20 minutes of stirring, 30 mM Na_2S solution was rapidly introduced, leading to the immediate formation of a pale-yellow CdS colloidal suspension. The mixture was further stirred for 1 hour to ensure complete precipitation. The obtained CdS QDs were separated by centrifugation, repeatedly washed with DI water and ethanol, and dried in an

oven at 80 °C for 6 hours to obtain a fine yellow powder. The successful synthesis and structural purity of CdS QDs were further confirmed using various characterization techniques.

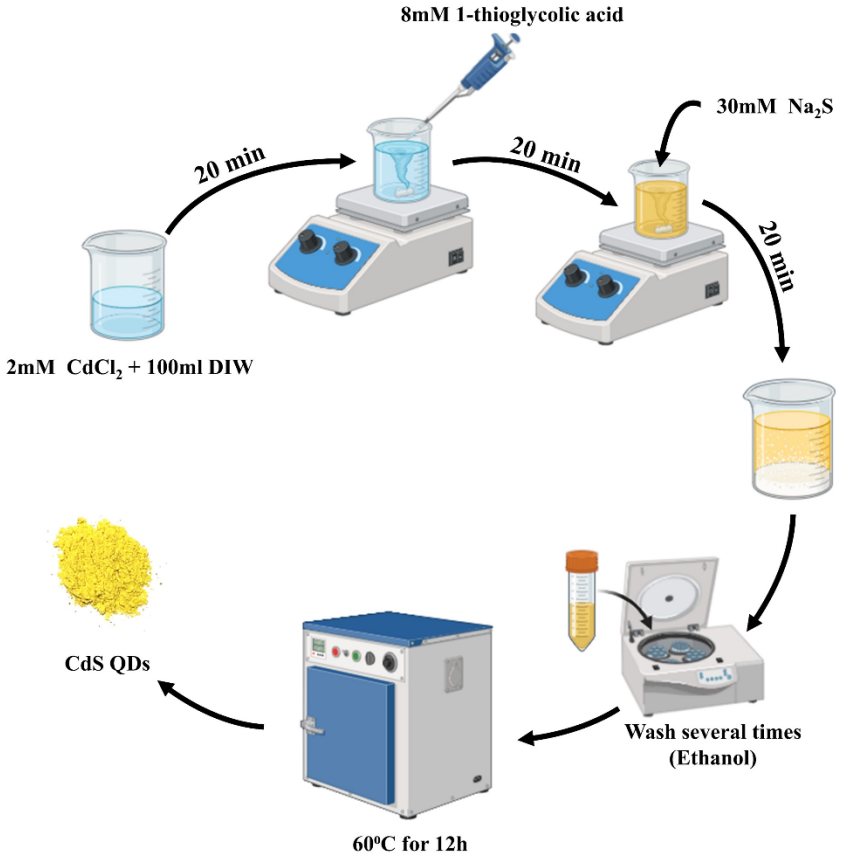

Scheme 1. Schematic illustration of experimental synthesis of CdS QDs *via* a wet-chemical precipitation route.

2.3 Computational Details:

The Quantum ESPRESSO (QE) package was used to perform first-principles calculations [16,17]. Ultrasoft pseudopotentials with valence electronic configurations of Cd: $4s^2 4p^6 4d^1 5s^2$, S: $3s^2 3p^4$, N: $2s^2 2p^3$, and O: $2s^2 2p^3$ were used to model electron–ion interactions [18]. The Perdew–Burke–Ernzerhof (PBE) functional was used in the GGA+U approach to treat exchange–correlation effects [19, 20]. Brillouin zone sampling was carried out using a 16 × 16 × 1 Monkhorst–Pack k-point grid [21] with Marzari–Vanderbilt smearing of 0.046 eV to improve convergence, and a plane-wave cutoff energy of 816 eV was used. Optimized norm-conserving pseudopotentials were

used to assess the optical properties, and the epsilon.x module was used for analysis [22,23]. The Hubbard U correction parameters were set to U_S = 4.2 eV for the S 3p orbitals and U_{Cd} = 4.0 eV for the Cd 4d orbitals [24,25], ensuring an accurate representation of electron localization and improved alignment with experimental observations. The geometry optimization was considered converged when the residual pressure reached –0.054 GPa and the total residual force was reduced to 0.04 eV Å^{-1}, confirming full structural relaxation. Bader charge analysis was performed using the Henkelman group's Bader code to quantitatively evaluate charge transfer between the gas molecule and the CdS sensing surface [26].

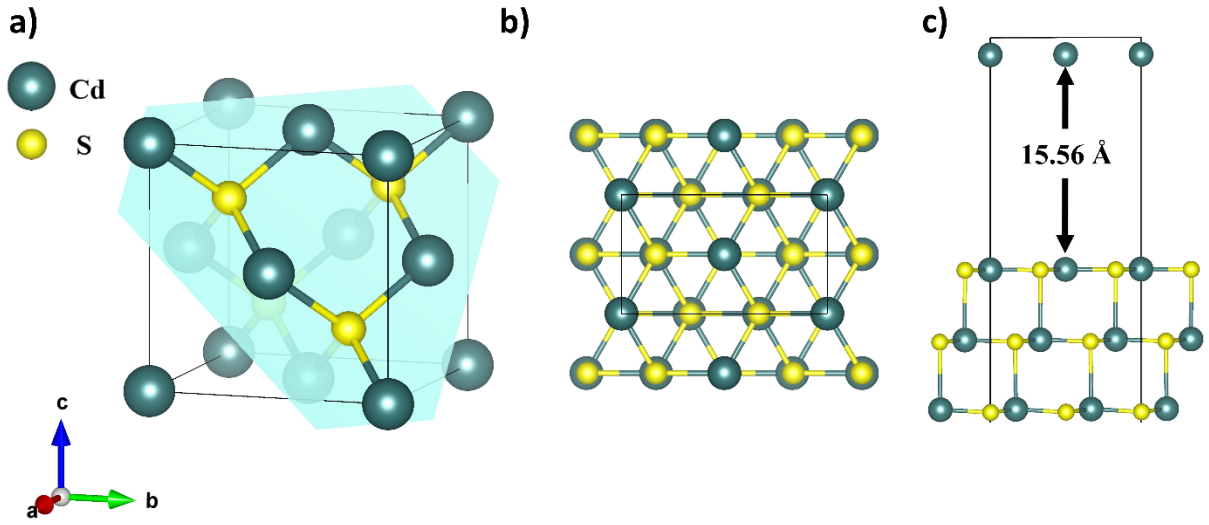

Figure 1. Optimized structures of a) bulk cubic CdS with highlighted (111) plane, b) Top view, and c) Side view of the CdS (111) surface.

The CdS surface was modeled as a periodic slab sliced along the (111) crystallographic orientation (Figure 1) [27]. The bulk CdS crystal structure represents cubic crystal geometry, with Cd and S atoms tetrahedrally attached (Figure 1a). The separation along the (111) plane yields a polar surface with alternating Cd- and S-terminated layers (Figure 1b), exposing both Lewis acidic (Cd) and Lewis basic (S) active sites, which are critical for gas adsorption and sensing performance. To avoid false interactions between periodic replicas, a vacuum layer of around 15 Å was introduced along the direction corresponding to the surface (Figure 1c). To avoid artificial interactions between periodic slab images, a vacuum layer of approximately 15 Å was introduced along the surface normal direction. Similar vacuum separations have been employed in previous CdS surface

adsorption studies to ensure sufficient decoupling between periodic replicas and reliable convergence of surface energetics [27]. Test calculations confirmed negligible changes in total energy and electronic structure upon further increasing the vacuum thickness, indicating that 15 Å provides adequate separation for accurate adsorption modeling. The slab was built with enough atomic layers to maintain bulk-like properties in the center while allowing full structural relaxation near the surface. The CdS (111) surface was selected because it is the thermodynamically stable and commonly exposed facet in cubic zinc-blende CdS nanocrystals. XRD and HRTEM analyses of the synthesized QDs indicate a dominant (111) orientation, confirming that this surface is representative of the experimentally prepared material. Therefore, modeling the CdS (111) surface provides a realistic and physically meaningful framework for investigating NO_2 adsorption behavior. This computational model offers a realistic environment for studying adsorption energetics, charge transfer mechanisms, electronic structural changes and sensing properties related to NO_2 sensing on the CdS (111) surface.

The adsorption energy (E_{ads}) was calculated using the following relation:

$$E_{ads} = E_{Total} - E_{surface} - E_{gas} \quad (1)$$

where E_{ads} is adsorption energy, E_{Total} is total energy of system (surface + gas), $E_{surface}$ total energy of surface (slab) and E_{gas} total energy of gas (NO_2) [28]. To determine the reaction kinetics, the activation energy (E_a)for adsorption and desorption processes was obtained using the climbing-image nudged elastic band (CI-NEB) method, which identifies the minimum energy pathway between the initial and final states of the reaction. The activation barrier corresponds to the energy difference between the transition state and the respective initial or final configuration:

$$E_a^{ads} = E_{TS} - E_{IS}\,, \quad E_a^{des} = E_{TS} - E_{FS} \quad (2)$$

where E_{TS} is the energy of the transition state along the reaction coordinate determined from the NEB calculations, E_{IS} corresponds to the energy of the gas molecule approaching the surface, and E_{FS} represents the energy of the adsorbed configuration. [29]

Charge transfer during gas adsorption was determined through Bader charge analysis [30], enabling accurate evaluation of electron redistribution between the gas molecule and the CdS sensing surface.

$$\Delta Q = Q_{total} - Q_{surface} \quad (3)$$

Where, Q_{total} is Total charge after gas adsorption and $Q_{surface}$ is charge of surface before gas adsorption.

The complex dielectric function ($\varepsilon(\omega)$) was evaluated according to:

$$\varepsilon(\omega) = \varepsilon_1(\omega) + i\varepsilon_2(\omega) \quad (4)$$

Where $\varepsilon_1(\omega)$ and $\varepsilon_2(\omega)$ are real and imaginary parts of dielectric function. The GGA+U computational approach enables an enhanced understanding of the material's optical behavior. namely $\varepsilon_2(\omega)$[31]

$$\varepsilon_2(\omega) = \frac{e^2\hbar}{\pi m^2\omega^2}\sum_{V,C}\int |M_{CV}(k)|^2\,\delta\{\omega_{CV}(k) - \omega\}\,d^3k \quad (5)$$

Where, $M_{cv}(k)$ is initial Brillouin zone which give by,

$$M_{cv} = \langle u_{ck}|e.\nabla|u_{vk}\rangle \quad (6)$$

where $\boldsymbol{e}$ denotes the electric field vector, indicating the direction associated with the electric potential. where u_{ck} and u_{vk} denote the periodic parts of the Bloch wave functions corresponding to the conduction and valence bands, respectively, and $\hbar\omega_{CV} = E_{Ck} - E_{Vk}$ represents the interband transition energy at a given k-point. [31]

The real component of the dielectric function, $\varepsilon_1(\omega)$, was derived from the imaginary component $\varepsilon_2(\omega)$ through the Kramers–Kronig transformation [32]. Mathematically,

$$\varepsilon_1(\omega) = 1 + \frac{2}{\pi}P\int_0^{\infty}\frac{\omega'\varepsilon_2(\omega')}{\omega'^2 - \omega^2 + i\eta}d\omega' \quad (7)$$

where P represents the integral's principal value, and η represents an infinitesimal number.

The optical constants, together with absorption coefficient α(ω), loss function L(ω), extinction coefficient κ(ω), refractive index n(ω), reflectivity R(ω), and optical conductivity σ(ω), were determined using the real and imaginary components of the dielectric function, $\varepsilon_1(\omega)$ and $\varepsilon_2(\omega)$. Their values were calculated using the standard relations listed below, with symbols given in standard notation. [33]

$$\alpha(\omega) = \left[\sqrt{\varepsilon_1^2(\omega) + \varepsilon_2^2(\omega)} - \varepsilon_1(\omega)\right]^{\frac{1}{2}} \tag{8}$$

$$L(\omega) = \frac{\varepsilon_2(\omega)}{\varepsilon_1^2(\omega)+\varepsilon_2^2(\omega)} \tag{9}$$

$$\kappa(\omega) = \frac{\sqrt{-\varepsilon_1(\omega)\sqrt{\varepsilon_1^2(\omega)+\varepsilon_2^2(\omega)}}}{2} \tag{10}$$

$$n(\omega) = \frac{\left[\sqrt{\varepsilon_1^2(\omega)+\varepsilon_2^2(\omega)}+\varepsilon_1(\omega)\right]^{\frac{1}{2}}}{\sqrt{2}} \tag{11}$$

$$R(\omega) = \frac{n^2-1}{n^2+2} \tag{12}$$

$$\sigma(\omega) = \omega\varepsilon_0\varepsilon_2(\omega) \tag{13}$$

In sensing prospective the sensing response (S) and characteristic time (τ) (is inverse of the rate constant and indicates how quickly a gas molecule adsorbs (response) or desorbs (recovery) from the sensor surface.) were calculated using following equations [34]

$$S = e^{\frac{|\Delta E_g|}{kT}} \tag{14}$$

$$\tau_{response} = \frac{1}{\upsilon_o} e^{\frac{\left|-E_a^{ads}\right|}{kT}}, \tau_{recovery} = \frac{1}{\upsilon_o} e^{\frac{\left|-E_a^{des}\right|}{kT}} \tag{15}$$

Where ΔE_g is band gap energy, E_{ads} adsorption energy, $\frac{1}{v_o}$ attempt frequency (10^{12}), k is Boltzmann constant and T is working temperature respectively.

2.4 Gas Sensing Measurement:

Gas-sensing performance was evaluated with a static sensing setup (Figures S1). Electrical connections were built to a base plate containing an integrated heating element for temperature control. A chromel-alumel (Cr-Al) thermocouple connected to a digital controller kept the temperature under control. The target gas was put into the chamber with a precision syringe. Aluminum electrodes were used to make an ohmic contact, and the sensor received a continuous DC bias. The resulting current response was measured with a digital picoampmeter. After each measurement cycle, dry air was evacuated into the chamber to restore baseline conditions.

2.5 Material Characterization

The formation and properties of CdS QDs were confirmed using a range of characterization techniques. X-ray diffraction (XRD) was performed using a Bruker AXS D8 ADVANCE diffractometer (Germany) to determine the crystalline phase and estimate the crystallite size. Crystal structure and lattice fringes were further investigated using high-resolution transmission electron microscopy (HRTEM) and selected area electron diffraction (SAED) on a JEOL JEM-2100 Plus instrument. Field-emission scanning electron microscopy (FESEM; FEI Nova NanoSEM 450) coupled with energy-dispersive X-ray (EDAX/EDS) analysis, was used to investigate surface morphology and determine elemental composition. Raman spectroscopy, carried out using a Renishaw micro-Raman spectrophotometer, was used to analyze vibrational characteristics and further validate the structural features. The elemental composition and chemical states were examined using X-ray photoelectron spectroscopy (XPS; PHI 5000 VersaProbe III). UV–Visible absorption spectra were recorded using a JASCO V-750 spectrophotometer in the range of 200–800 nm to evaluate the optical absorption characteristics and estimate the optical bandgap. Steady-state photoluminescence (PL) spectra were recorded using an FLS100 spectrometer to probe electron–hole recombination behavior, whereas time-resolved photoluminescence (TRPL) measurements were performed to determine carrier lifetime dynamics and evaluate recombination kinetics. Finally, surface area and pore size distribution were analyzed

via the Brunauer–Emmett–Teller (BET) method using a Beckman Coulter Nova 1200e sorption analyzer, based on nitrogen adsorption at liquid nitrogen temperature with a precision of 98%.

3. Results and Discussion

3.1 Characterization details

The structural properties of CdS QDs were examined using X-ray Diffraction (XRD) (Figure 2a). The diffraction pattern exhibits peaks at 2θ values of 27.05°, 44.42°, and 52.03°, corresponding to the (111), (220), and (311) planes of the cubic zinc blende structure [35], consistent with the standard reference (PCPDF#00454). The peaks are well matched to the pure face-centered cubic (fcc) phase with space group F-43m and lattice parameter a=5.818 Å. The absence of extra peaks confirms the high purity of the QDs, free from detectable impurities.

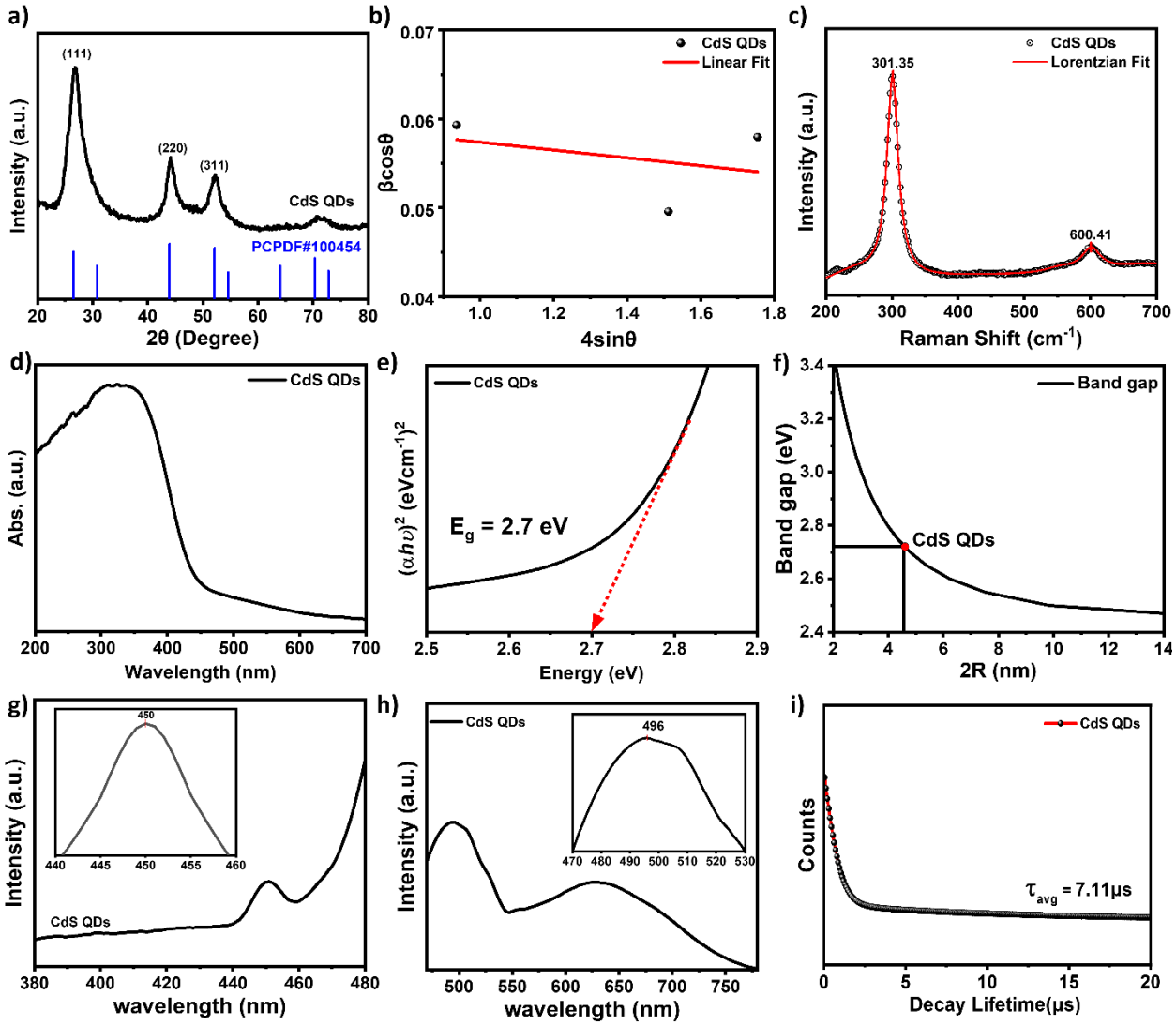

Figure 2. a) XRD pattern, b) Williamson Hall plot, c) Raman spectra, d) UV Vis absorption spectra, e) Tauc plot, f) EMA model, g) PL excitation spectra, h) PL emission spectra, i) Fluorescence decay spectra of CdS QDs.

The average crystallite size, estimated using the Debye Scherrer formula [36]:

$$D = \frac{k\lambda}{\beta cos\theta} \tag{16}$$

Where, k is shaping constant, λ is wavelength of source (Cu Kα = 1.54 Å), β is full width half maxima (FWHM) and θ is diffraction angle, an overall average of 4.61 nm. The broad nature of the peaks reflects the small particle size and good crystallinity. Using the Williamson-Hall (W-H) method, which considers contributions from both crystallite size and lattice strain [36]:

$$\beta cos\theta = 4\varepsilon sin\theta + \frac{k\lambda}{D} \tag{17}$$

the crystallite size (D) and microstrain (ε) were simultaneously estimated (Figure 2b). The W-H analysis gives an average crystallite size of 4.34 nm and microstrain 4.4, and a dislocation density of 5.3×10^{-2} nm^{-2}**,** confirming high crystallinity with minor lattice distortions.

The room temperature Raman spectrum of CdS QDs is shown in the figure 2c, fitted with Lorentzian function. It shows well resolved peaks at 300.81 and 600.80 cm^{-1} corresponding first order (1 LO) and second order (2 LO) scattering of longitudinal optical phonon modes. We observed perceptible asymmetry in the line shape due to phonon confinement effect. The peak has also slightly shifted to lower frequency as compared with the LO mode of bulk CdS which is observed at 305cm^{-1}[37]

UV-Vis absorption spectra of CdS QDs as shown in the figure 2d, The absorption peak of the bulk CdS was found to be around 512 nm which corresponds to energy band gap around 2.42 eV. The synthesized CdS QDs are blue shifted in comparison to the energy band gap of the bulk CdS 2.42 eV [37]. Due to quantum size confinement effect is blue shift of the optical absorption edge around 450 nm which shows that the formation of particles in the nanometer size regime. The optical band gap (E_g) of the materials was estimated using the Tauc plot method (figure 2e) [38], based on the equation:

$$(\alpha h\nu)^{\gamma} = A\left(h\nu - E_g\right) \tag{18}$$

where α is the absorption coefficient, h is Planck's constant, ν is the photon frequency, A is a proportionality constant, Eg represents the band gap energy, and γ denotes the nature of the electronic transition (γ = 1/2 for direct transitions and γ = 2 for indirect transitions). By extrapolating the linear region of the plot, the estimated band gap values are 2.72 eV for CdS QDs indicates the formation of nanosized quantum dots with size-dependent quantum confinement effects. The wavelength of the maximum exciton absorption decreases as the particle size decreases because of quantum confinement of the photogenerated electron-hole pairs [39]. L. Brus proposed the effective mass approximation model (EMA) to explain the theory of blue shift, which gives energy bandgap of CdS QDs as shown in the below equation [40]:

$$E_g^{QD}(R) = E_g + \frac{h^2\pi^2}{2R}\left[\frac{1}{m_e} + \frac{1}{m_h}\right] - \frac{1.78e^2}{\epsilon R} \tag{19}$$

Where $\hbar$ is Plank constant, R is the radius of QDs, m_e is effective mass of electron, m_h is effective mass of hole, ϵ is the dielectric constant of the material. In the equation the coulomb term of

electron hole interaction was small compared to the electron hole confinement kinetic energy, which gives support to the blue shift. Using the provided value of m_e and m_h of 0.2m and 0.8m where m is mass of free electron, we back calculated the QDs size to be 4.2 nm as shown in figure 2f [41].

The optical behavior of CdS QDs was studied using excitation, emission, and time-resolved photoluminescence (TRPL) spectroscopy. The PL excitation spectrum (Figure 2g) closely corresponds to the absorption edge seen in the UV-Vis analysis, showing effective photon absorption and demonstrating strong electronic coupling between the excitation and absorption processes. The emission spectra (Figure 2h) shows a broad band ranging from 440 to 530 nm, with greatest intensity around 500 nm. The red shift of the PL emission peak at 496 nm (Fig. 2h) compared to the excitation-related feature at 450 nm (Fig. 2g) can be attributed to defect-assisted radiative recombination. In CdS quantum dots, sulfur vacancies and surface trap states introduce shallow energy levels within the band gap. Radiative transitions from these localized states to the valence band occur at lower photon energies, resulting in a red-shifted emission relative to near-band-edge recombination. The blue shift seen in comparison to bulk CdS (515 nm) indicates the creation of nanoscale QDs due to quantum confinement phenomena. The broad spectral profile indicates the presence of shallow defect-related states that contribute to radiative recombination.

Time-resolved PL analysis (Figure 2i) reveals an average carrier lifetime of approximately 7.11 μs, which is considerably longer than the microsecond-scale lifetimes (1.3–1.7 μs) reported for PbS-based quantum dots in the literature [42]. The prolonged lifetime observed here suggests enhanced carrier localization and reduced non-radiative recombination pathways, possibly associated with surface passivation and trap-state-mediated recombination. The decay profile was best fitted using a bi-exponential function, indicating the coexistence of fast band-edge recombination and slower trap-assisted processes. Such microsecond-scale lifetimes strongly suggest that the recombination process is mostly mediated by surface trap states rather than direct band-edge transitions. This finding is consistent with prior studies that linked long-lived PL emissions to sulfur vacancy-derived deep trap states on the CdS surface. The longer lifetime is beneficial for charge separation and charge-carrier retention, which could improve sensing and

photocatalytic activity; nevertheless, excessive trap-state dominance may result in greater nonradiative losses [43].

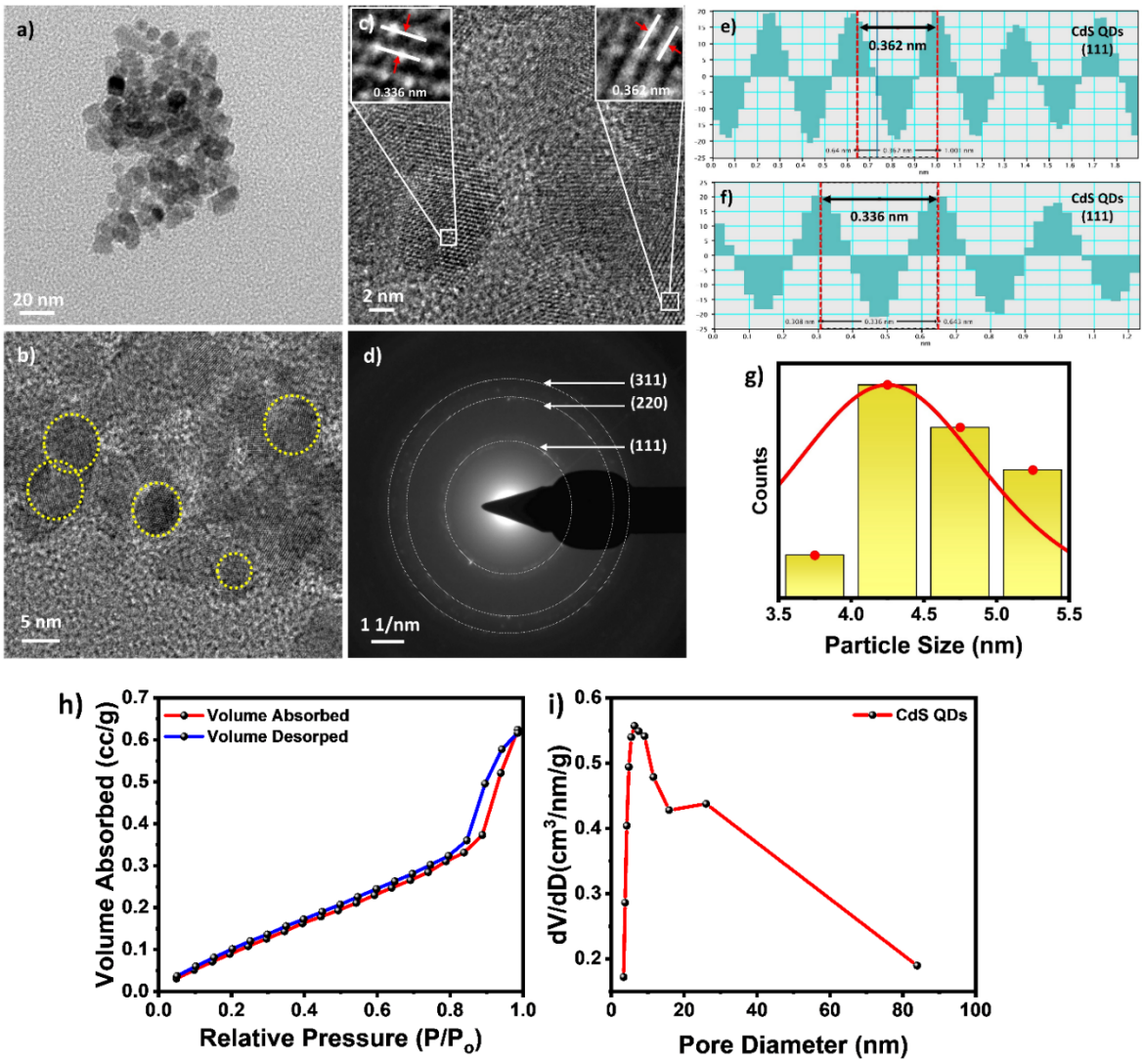

Figure 3. a-b) Low-magnification TEM image, c) HRTEM images, d) SAED pattern, e–f) Intensity-profile of HRTEM images, g) Particle-size histogram h) N_2 adsorption–desorption isotherms, and i) BJH pore-size distributions of CdS QDs.

The morphological and compositional characteristics for CdS QDs were investigated using FESEM and EDS. The low-magnification FESEM image (Figure S2a) reveals irregularly shaped, agglomerated nanoparticles, typical of high surface energy in nanoscale systems. At higher magnifications (Figures S2b–c), CdS QDs exhibit a rough and porous morphology with fissures

likely arising from rapid nucleation and growth. The highest-resolution image (Figure S2d) shows nanoscale ridge-like and layered features, suggesting a crystalline or partially ordered structure. EDS analysis (Figure S2e) confirms the presence of only cadmium and sulfur, with atomic weight percentages of Cd = 44.46% and S = 55.54%, consistent with near-stoichiometric CdS composition. Elemental mapping (Figure S2f), along with the individual Cd (Figure S2g) and S (Figure S2h) maps, demonstrates a uniform and co-localized distribution of the constituent elements across the material. These observations validate that the wet-chemical synthesis route effectively yields homogeneous, phase-pure CdS QDs without detectable elemental segregation.

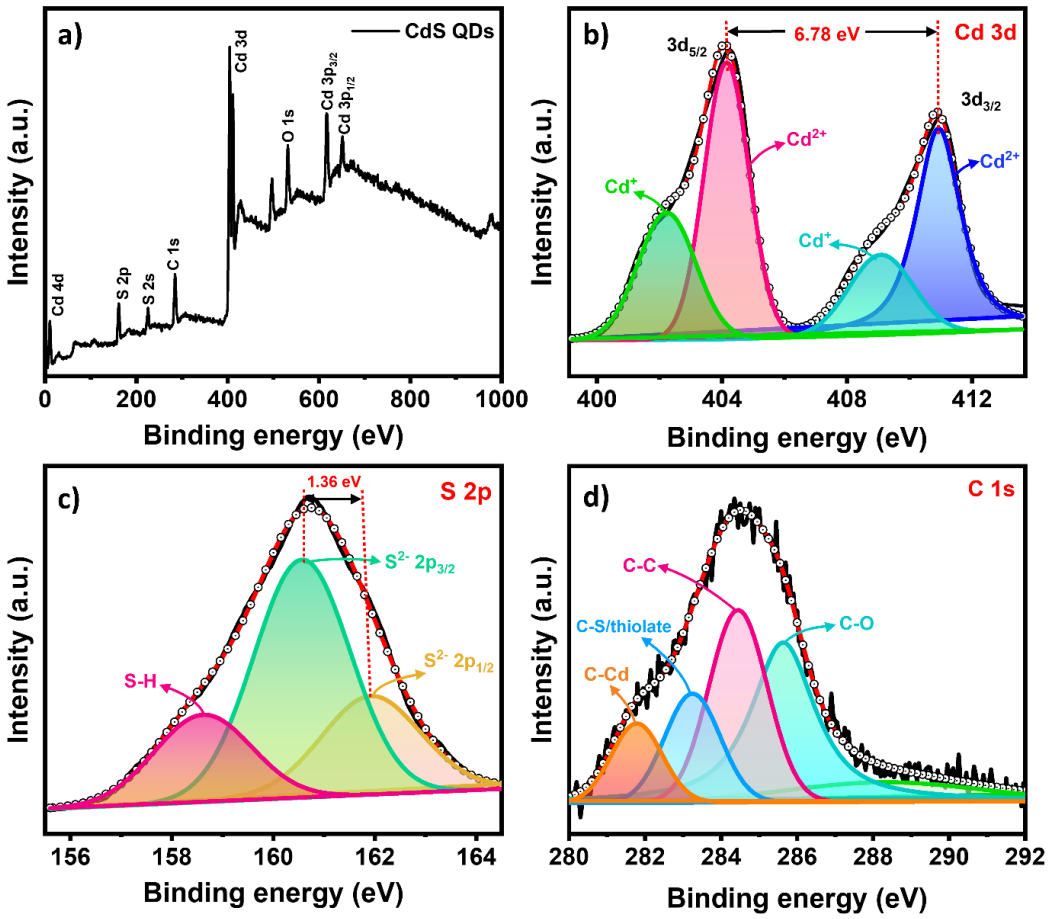

Figure 4. a) XPS survey spectrum of CdS QDs, b) deconvoluted Cd 3d, c) deconvoluted S 2p, d) C1s spectra of CdS QDs

The shape and crystallinity of the CdS QDs were investigated using high-resolution transmission electron microscopy (HRTEM). Agglomerated nanoparticles are visible in the low-magnification TEM picture (Figure 3a), which is characteristic of quantum dots because of their high surface

energy. Interconnected nanocrystals with uneven borders are seen in the medium-magnification image (Figure 3b). Distinct lattice fringes with interplanar spacings of 0.336 nm and 0.362 nm, which correspond to the (111) crystal planes of cubic CdS, can be identified at higher resolution (Figure 3c). The high crystallinity of the quantum dots is confirmed by the concentric diffraction rings indexed to the (311), (220), and (111) planes in the selected-area electron diffraction (SAED) pattern (Figure 3d) [44]. The predicted fringe spacings of 0.362 nm and 0.336 nm, which further support the preferred CdS (111) crystal orientation, are validated by intensity-profile studies calculated from the HRTEM lattice areas (Figures 3e–f) [45]. A smaller size range centered around 4–5 nm is shown by the particle size distribution (Figure 3g), which was fitted using a Gaussian model. HRTEM and SAED data confirm that the synthesized CdS QDs are well-crystallized, with consistent lattice parameters and a relatively uniform nanoscale size distribution, in agreement with XRD and Raman analyses.

The nitrogen adsorption-desorption isotherm of CdS QDs (Figure 3h) shows a type IV profile with a H_3-type hysteresis loop at higher relative pressures ($P/P_0 > 0.85$), which is characteristic of mesoporous materials generated through interparticle aggregation [46]. BET analysis showed a surface area of 5.895 m^2/g and a total pore volume of 0.0158 cm^2/g, indicating a moderately porous surface. The BJH pore-size distribution (Figure 3i) shows an average pore diameter of about 3.38 nm, indicating the occurrence of tiny mesopores toward the lower mesoporous limit. This well-defined nanoscale porosity allows for rapid gas diffusion while also providing a huge number of active adsorption sites. Surface characteristics, along with quantum-confined particle size, improve surface reaction kinetics and charge transfer during gas interaction, leading to improve NO_2 sensing performance. [47]

X-ray photoelectron spectroscopy (XPS) was used to analyze the composition and oxidation states of the synthesized CdS QDs, as illustrated in Figure 4(a–d). The synthesis of CdS QDs without any significant impurity peaks is confirmed by the survey spectrum (Figure 4a), which shows the existence of Cd 4d, Cd 3d, S 2p, S 2s, C 1s, and O 1s signals [48]. Cadmium is mostly found in the +2-oxidation state, as confirmed by the high-resolution Cd 3d spectrum (Figure 4b), which shows two peaks at roughly 405.0 eV ($3d_{3/2}$) and 411.8 eV ($3d_{1/2}$), separated by 6.78 eV, indicating of Cd^{2+} in CdS QDs. This verifies that cadmium exists primarily in the +2-oxidation state. The S 2p spectrum (Figure 4c) shows the characteristic sulfide doublet at 161.3 eV ($2p_{3/2}$) and 162.6 eV

($2p_{1/2}$), equivalent to S^{2-} in CdS. A small peak near ~160 eV indicates sulfur-rich or nonstoichiometric species, probably caused by adsorbed S-H groups [48]. The C 1s spectra (Figure 4d) exhibits peaks at 284.6 eV (C-C/C=C), 285.7 eV (C-O), and 283.3 eV, corresponding with C-S or C-Cd bonding, suggesting that organic surface ligands utilized during synthesis are partially connected to the QDs. These carbon and oxygen-related characteristics are attributable to residual capping agents or adsorbed species on the surface. The Cd 3d, S 2p, and C 1s spectra confirm the effective synthesis of Cd^{2+}-S^{2-} CdS QDs with surface ligand components [48].

3.2 Theoretical understanding of NO_2 adsorption

To gain more understanding of the adsorption mechanism at the CdS-NO_2 interface, the most stable configuration of NO_2 adsorbed via its nitrogen atom onto the CdS (111) surface was studied. After relaxing, the nitrogen atom stabilizes at an equilibrium distance of 2.89 Å from the nearest surface Cd atom, with little structural change. The intrinsic N-O bond lengths (1.21-1.23 Å) are similar to gas-phase values, showing minimal deformation of the NO_2 molecule during adsorption.

The Cd atom interacting with the adsorbate shifts slightly outward by 0.05-0.10 Å, but the surrounding S atoms move by less than 0.02 Å, indicating negligible lattice disturbance. This structural stability is also corroborated by the charge density difference isosurface (insight Figure 5a), which shows electron accumulation (yellow) and depletion (blue) regions with weak interaction caused mostly by long-range charge redistribution rather than strong bond formation. Charge density difference mapping gives additional details on the electronic effects of adsorption. The pristine CdS (111) surface 2D electron density pattern (Figure S3c) demonstrates consistent charge dispersion prior to contact. After attaching NO_2 to the Cd site (Figure 5c), electrons accumulate around the NO_2 molecule and depletion near the surface Cd atoms. These polarization-induced changes extend slightly beyond the surface and into the vacuum region, suggesting an indirect, surface-mediated electron-transfer mechanism that is more typical of weak physisorption than chemisorption [49].

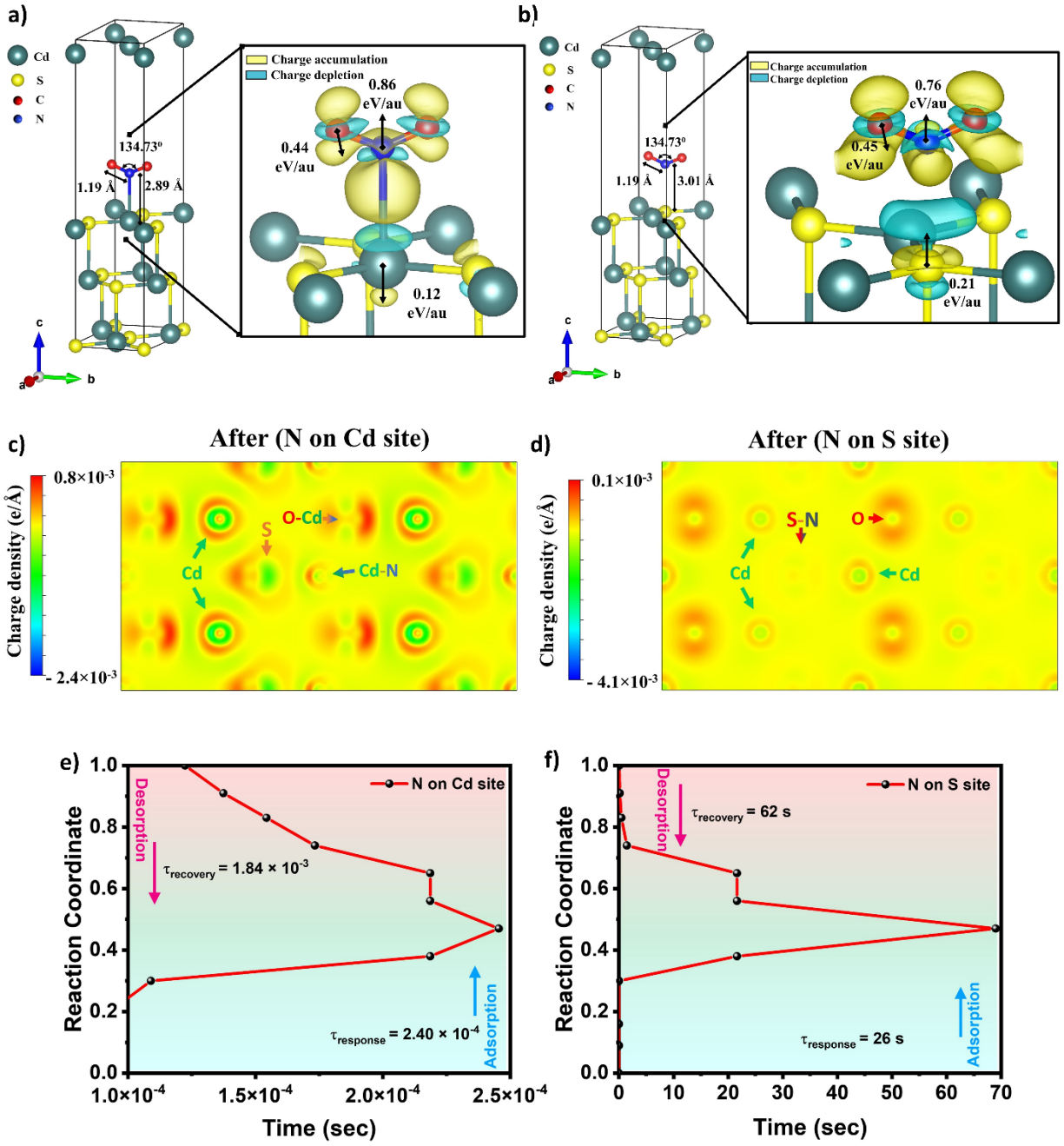

Figure 5. Charge density difference isosurface for N adsorption on the a) Cd site, b) S site, 2D charge density deference map c) on Cd site, d) on S site and theoretical response-recovery time profiles for N on e) Cd site, f) S site of the CdS (111) surface.

To understand the better adsorption behavior of NO_2 at the S-terminated CdS (111) surface, we determined the best possible geometry of the nitrogen-mediated configuration (N-on-S).

Relaxation causes the nitrogen atom to approach the surface S at a shorter distance (3.01 Å) than in the N-on-Cd arrangement, indicating greater orbital overlap. Minor intramolecular deformation, including asymmetric elongation of N-O bonds and 1-2°, indicates a shift towards chemical interaction. The surface sulfur atom shifts inward by 0.06-0.12 Å, while surrounding Cd atoms experience modest lateral displacements, indicating local lattice relaxation and partial electronic rehybridization (Figure 5b).

Charge-density-difference analysis (Figure 5d) shows significant electron accumulation in the S-N contact region and depletion around the S-3p orbitals, demonstrating direct charge donation from the CdS surface to NO_2 molecules. The complementary 2D Charge-density-difference map (Figure 5c) indicates localized polarization that reaches slightly beyond the surface, indicating more selective and localized bonding than the diffuse interaction seen in the N-on-Cd example. The nitrogen atom receives residual forces of 0.041-0.048 eV $Å^{-1}$, while surface sulfur and nearby Cd atoms show values of 0.02-0.03 eV $Å^{-1}$. Subsurface atoms are hardly impacted (<0.01 eV $Å^{-1}$). These results demonstrate that the N-on-S arrangement promotes a more powerful and chemically selective adsorption mechanism, which is controlled by direct lone-pair donation and localized structural adaptation [49].

Optimized structures for O-on-Cd and O-on-S adsorption configurations show two different interactions between NO_2 and the CdS (111) surface. In the O-on-Cd configuration (Figure S3a), the oxygen atom approaches the surface Cd site, forming a fairly strong Cd-O coordination. The Cd-O distance contracts dramatically from its original vertical position, and local relaxation spreads into the first coordination shell, leading nearby S atoms to move somewhat outward. Surface Cd acts as an electron-deficient Lewis center, interacting with NO_2 oxygen. In contrast, the O-on-S configuration (Figure S3b) maintains a substantially larger equilibrium gap between the O atom and the surface S, with the molecule positioned higher above the surface plane and causing relatively minor distortion. The low displacement of S atoms suggests that S sites do not have a strong interaction with O-terminated NO_2. Force analysis confirms the various interaction strengths. In the O-on-Cd instance, the Cd atom directly engaged shows moderate residual forces of 0.05-0.07 eV $Å^{-1}$, but surrounding S atoms show relatively small force components as equilibrium is established. In the O-on-S example, forces are less than 0.02 eV $Å^{-1}$, indicating a slight physisorptive interaction that is not affecting the CdS lattice. Charge-density-difference

isosurface plots (Figure S3a) show well-defined charge accumulation around the oxygen atom, as well as depletion near the surface Cd, indicating partial hybridization of O-2p orbitals with electron-deficient Cd states. The 2D Charge-density-difference slice after adsorption on Cd (Figure S3d) shows localized and asymmetric charge redistribution centered along the Cd–O axis. In contrast, the 2D charge map of the pristine surface (Figure S3d) and the O-on-S configuration (Figure S3e) display only weak, diffuse polarization without a distinct bonding lobe, confirming the absence of significant orbital overlap or chemical bonding in the O-on-S configuration [50].

Table 1. NO_2 adsorption on CdS (111) at different binding sites.

Substrate	Adsorption Site	Shortest Molécule–Surface Distance (Å)	Adsorption Energy (eV)	Interpretation
CdS (111)	**N on Cd**	2.89 Å	−0.14	Very weak physisorption; weak charge transfer.
	N on S	3.01 Å	−0.88	Strongest adsorption; chemisorption
	O on Cd	2.59 Å	−0.32	Weak-to-moderate bonding; O interacts weakly with Cd, limited hybridization.
	O on S	2.61 Å	−0.57	Moderate adsorption; O–S interaction stronger than O–Cd but weaker than N–S.

The adsorption energies (Table S1) (Figure S4a) show that NO_2 interacts more strongly with surface sulfur atoms than cadmium. N-on-S has the highest adsorption energy (-0.88 eV), followed by O-on-S (-0.57 eV), O-on-Cd (-0.32 eV), and N-on-Cd (-0.14 eV). Because oxygen has a higher electron affinity, it adsorbs slightly more strongly than nitrogen at the same site. The low magnitudes of E_ads indicate weak chemisorption or physisorption, which matches the minimal structural and electronic perturbations observed [51]. The interaction trend (N-on-S > O-on-S > O-on-Cd > N-on-Cd) shows that NO_2 preferentially adsorbs at S-rich surface regions, significantly contributing to the valence band. This site selectivity is highly relevant for sensing applications,

as stronger adsorption at S sites induces more pronounced charge redistribution, thereby enhancing the sensitivity of CdS-based sensors toward NO_2.

The adsorption properties of NO_2 on various CdS (111) surface binding sites are shown in Table 1. Despite a slightly greater molecule–surface separation (3.01 Å), nitrogen adsorption on the S site has the highest adsorption energy (–0.88 eV), showing chemisorption driven by substantial N–S electronic hybridization. On the other hand, nitrogen adsorption on the Cd site confirms physisorption and restricted charge interaction with a shorter separation of 2.89 Å and very weak binding (–0.14 eV). When it comes to oxygen adsorption, the O-on-Cd configuration shows moderate interaction (–0.32 eV, 2.59 Å), while the O-on-S model shows stronger adsorption (–0.57 eV) with an equivalent separation of 2.61 Å. These results demonstrate that the active site and adsorption atom have a substantial impact on adsorption behavior, with sulfur sites often encouraging stronger contact and more noticeable electronic disturbance than cadmium sites. This offers important information about how adsorption preferences affect charge transfer properties and sensing efficiency.

The Bader charge analysis (Table S2) shows that electron flow from CdS to NO_2 is very site-dependent. N-on-S has the highest electron gain by the NO_2 molecule (+2.595 e), indicating substantial chemisorption due to effective overlap between the nitrogen lone-pair orbital and the S-3p states. In contrast, N-on-Cd exhibits negligible charge gain (+0.040 e), indicating a weak contact similar to physisorption [52]. Oxygen-mediated adsorption is also weak, with O-on-Cd and O-on-S yielding just +0.053 and +0.048 e, respectively, due to oxygen's strong electronegativity, which limits additional electron transfer. Bader charge analysis reveals that the N-on-S arrangement significantly improves NO_2 sensing responsiveness. This occurs when electrons are extracted from the CdS surface, causing charge depletion and increased resistance, which is consistent with CdS behavior as an n-type semiconductor. The substantial charge transfer predicted for S-site adsorption indicates significant electron withdrawal from the n-type CdS surface, resulting in pronounced resistance modulation. This theoretical finding directly correlates with the experimentally observed high NO_2 sensitivity, as greater electron depletion from the conduction band enhances the change in resistance. In contrast, the comparatively small charge transfer at Cd sites explains the weaker resistance modulation but contributes to faster response–recovery dynamics.

Table 2. Calculated activation energies for adsorption and desorption (E_a^{ads} and E_a^{des}), response time ($\tau_{response}$), recovery time ($\tau_{recovery}$) at 125 °C, and sensing response (S) for different NO_2 adsorption configurations on the CdS surface slab.

Site	E_a^{ads}	E_a^{des}	$\tau_{response}$ at 125 °C (s)	$\tau_{recovery}$ at 125 °C (s)	S
N on Cd	0.03 eV	0.10 eV	2.40×10^{-4}	1.84×10^{-3}	3×10^{13}
O on Cd	0.09 eV	0.21 eV	1.64×10^{-3}	0.34	5.4×10^{4}
O on S	0.24 eV	0.38 eV	0.9	2.2	3.3×10^{9}
N on S	0.34 eV	0.36 eV	26	62	1×10^{4}

Table 2 shows that adsorption configuration significantly affects adsorption activation energy (E_a^{ads}), desorption activation energy (E_a^{des}), characteristic time (τ), and sensing response (S) for different NO_2 adsorption configurations on the CdS (111) surface. The results indicate that the adsorption configuration strongly influences both the thermodynamic stability and the kinetic behavior of the sensing process. Nitrogen adsorption on the Cd site (N on Cd) exhibits the highest sensing response (3×10^{13}), indicating that Cd atoms serve as the most active adsorption centers for NO_2 detection. In contrast, nitrogen adsorption on the S site (N on S) shows significantly lower sensing response (1×10^{4}), suggesting comparatively weaker interaction with the surface. Oxygen-based adsorption configurations demonstrate intermediate sensitivity, where O on S (3.3×10^{9}) shows substantially higher sensing response than O on Cd (5.4×10^{4}), further highlighting the crucial role of Cd surface sites in enhancing sensing performance [52].

The reaction kinetics were analyzed using activation energies obtained from the climbing image nudged elastic band (CI-NEB) calculations, which determine the minimum energy pathway between the initial and final adsorption states. The NEB energy profiles presented in Figure S5a reveal the transition states and corresponding activation barriers for NO_2 adsorption on different surface sites. Among the investigated configurations, the N on Cd arrangement exhibits the lowest adsorption activation energy (E_a^{ads} = 0.03 eV) shown in Figure 5e, resulting in an ultrafast response time of 2.40×10^{-4} and a recovery time of 1.84×10^{-3} s at 125 °C. In comparison, O on Cd and O on S configurations possess moderately higher activation barriers (0.09 - 0.24 eV) (Figure

S5b-S5c), leading to slower response times of 1.64×10^{-3} s and 0.9 s, respectively. The N on S configuration exhibits the highest adsorption barrier (0.34 eV) shown in Figure 5f, which results in the slowest response and recovery times of 26 s and 62 s, respectively, indicating stronger adsorption but slower reaction kinetics. The theoretical response–recovery behavior derived from the Cl-NEB-based kinetic analysis, where the evolution of the reaction coordinate with time clearly distinguishes the adsorption and desorption processes for different adsorption sites. These results demonstrate that Cd surface atoms provide highly active adsorption centers with rapid sensing kinetics, whereas S sites contribute to relatively stronger adsorption but slower recovery behavior. The combined analysis of adsorption energetics and reaction kinetics indicates that the CdS (111) surface possesses favorable characteristics for efficient NO_2 sensing at elevated temperatures such as 125 °C [52].

The projected band structure of the pristine CdS (111) surface (Figure S6a) shows a distinct bandgap with no defect-related mid-gap states, indicating inherent electronic stability. The valence band maximum (VBM) is primarily made up of S-3p states, whereas the conduction band minimum (CBM) is formed by Cd-5s/5p orbitals [49]. The Fermi level is near to the CBM, as expected given CdS n-type nature. N-on-Cd introduces mild N-2p contributions near the VBM upon NO_2 adsorption via nitrogen (Figures 6a and 6b), creating shallow acceptor-like states with a little downward shift in the Fermi level. N-on-S, on the opposite hand, causes stronger N-2p/S-3p hybridization, resulting in localized states just above the VBM, lowering the effective bandgap and producing a more noticeable Fermi-level shift, which is a sign of increased carrier localization and electron withdrawal [49]. For oxygen-dependent adsorption (Figures S6b and S6c), O-on-Cd produces deeper O-2p-derived impurity states near the VBM through hybridization with Cd orbitals, narrowing the bandgap and decreasing the Fermi level. O-on-S causes the most severe disruption to the band structure, resulting in the creation of deep mid-gap states, reduced band dispersion, large charge redistribution, and the greatest downward Fermi-level shift. This points to dominating carrier trapping and the most evident acceptor behavior across all adsorption methods [52].

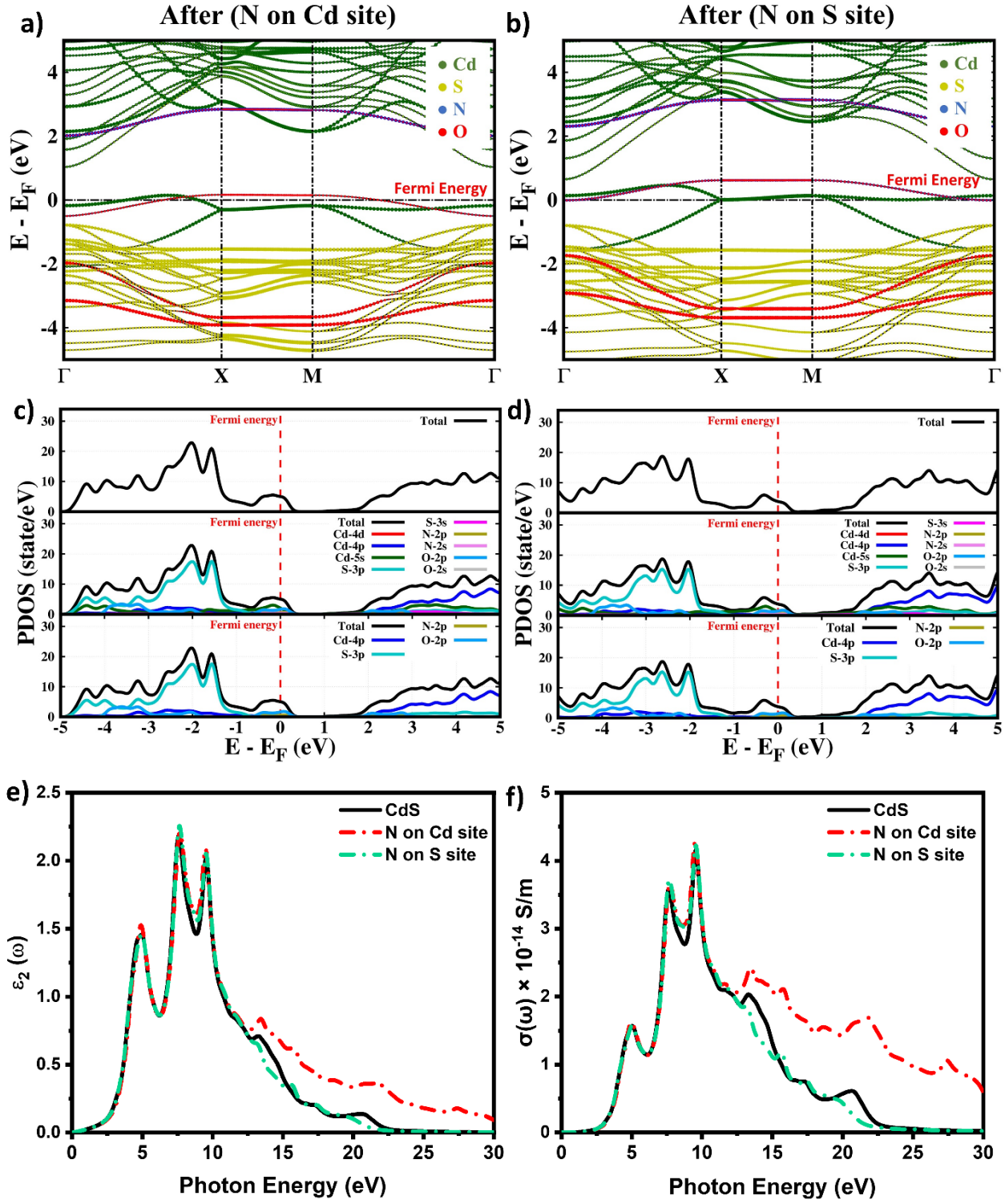

Figure 6. Projected band structure of N adsorption on a) Cd site b) S site, Partial density of state of N adsorption on c) Cd site d) S site, e) imaginary part of dielectric function f) optical conductivity of CdS (111) surface.

The projected density of states (PDOS) of the pristine CdS (111) surface (Figure S6d) reveals a distinct semiconductor profile with a low DOS at the Fermi level (0 eV). The valence band is dominated by Cd-5s/4d/4p and S-3s/3p states, whereas the conduction band is predominantly composed of Cd-5s/5p orbitals. There are no N or O contributions, which confirms the absence of defect-induced mid-gap states. Nitrogen adsorption (Figures 6c and 6d) results in the formation of new Fermi-level occupied states. For N-on-Cd, a sharp N-2p peak at 0 eV generates defect-induced states that might reduce the bandgap or cause partial oxidation, with minor N-2s contributions and minimal disruption to Cd and S states. In N-on-S, N-2p states form around the Fermi level and hybridize with S-3p/3s orbitals, resulting in modest electronic disruption while keeping the original valence band structure [49]. Oxygen adsorption (Figures S6e and S6f) introduces vacancy donor-like states above the Fermi level. O-on-Cd exhibits a prominent O-2p peak at +0.3 eV, while O-on-S exhibits a larger peak at +0.5 eV, indicating increased disturbance near the conduction band edge. These changes indicate the possibility of higher Fermi-level movement and enhanced carrier concentration. The Cd and S orbital frameworks remain relatively intact in all configurations, with the principal electronic changes resulting from N-2p and O-2p interactions [52].

In Figure S7a, the real part of the dielectric function ($\varepsilon_1(\omega)$) for pristine CdS shows a large positive range from 0-3 eV, with peaks at 3.5 eV and 8.5 eV, followed by a minimum near 10 eV and a progressive climb approaching at 30 eV Adsorption on Cd sites (N-on-Cd and O-on-Cd) modestly increases ε_1 in both peak regions and the high-energy range (10-20 eV), showing higher surface polarizability due to small charge transfer. Adsorption on S sites results in smaller changes, indicating weaker interactions with the surface. In Figure 6e, the imaginary part ($\varepsilon_2(\omega)$) related to optical absorption reveals dominant peaks at 4.5 eV and 9.5 eV for pristine CdS, with a secondary feature about 6.5 eV. NO_2 adsorption causes an increase in ε_2 at 13 eV for Cd-site adsorption, indicating more permitted transitions due to NO_2-induced electronic states. S-site adsorption results in a smaller perturbation. These improvements suggest more efficient photoexcited charge creation, which is useful for optoelectronic and photoelectrochemical NO_2 sensing [53].

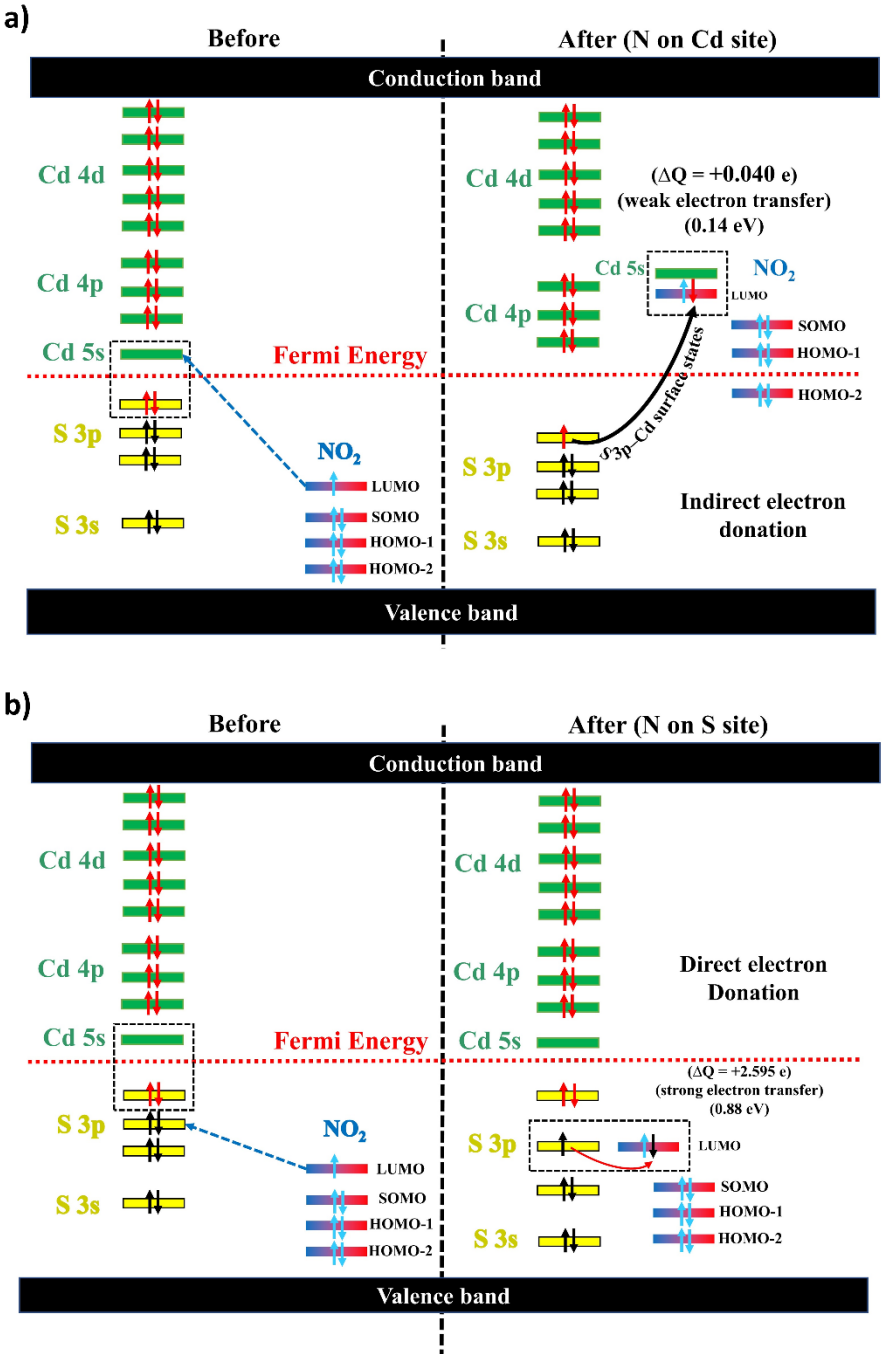

Figure 7. Mechanism of NO_2 Interaction and Charge Transfer on a) Cd site b) S site of CdS (111) surface.

The refractive index (n(ω)) (Figure S7b) rises sharply from 0-8 eV and peaks at the band-edge transition (4-5 eV). NO_2 adsorption on Cd sites causes a moderate rise in n(ω) in the 8-20 eV region, indicating improved polarizability, while S-site adsorption had no effect. At more than 20

eV, all curves converge (n = 0.8-0.9), demonstrating the supremacy of intrinsic lattice response [54]. The extinction coefficient (κ(ω)) (Figure S7c) is zero below the bandgap and has characteristic CdS peaks about 7-8 eV. Cd-site adsorption enhances these peaks and maintains greater κ at more 20-eV due to NO_2-induced optical transitions, meanwhile S-site adsorption has minimal effect. Reflectivity spectra (Figure S7d) indicate minor variations for Cd-site adsorption but a larger decrease (14-16 eV) for S-site adsorption, indicating higher local surface polarization. The loss function shown in figure S7e confirms these trends: N-on-S has a sharper and more intense primary plasmon peak (15 eV), indicating better charge-transfer coupling, whereas N-on-Cd broadens and weakens the plasmon signal [53]. The absorption coefficient (α(ω)) of pristine CdS shown in figure S7f substantial intrinsic absorption between 5-12 eV. Cd-site adsorption broadens the spectrum and boosts high-energy absorption (15–25 eV), suggesting additional optical transition pathways. In contrast, S-site adsorption decreases high-energy absorption due to electronic charge localization [53].

The optical conductivity σ(ω) (Figure 6f) shows the effects of adsorption geometry on sensing efficiency. Pristine CdS shows significant σ(ω) in the 8-12 eV range due to intrinsic inter-band transitions [55]. NO_2 adsorption on Cd sites considerably increases σ(ω) at 15-25 eV, indicating the creation of delocalized electronic states and increased charge mobility. This allows fast sensing, especially under light activation. Adsorption on S sites reduces σ(ω) above 15 eV due to increased charge localization from chemisorption, which enhances electron trapping and improves sensitivity in dark environments. Thus, Cd-site interactions promote rapid response and recovery, whereas S-site adsorption improves detection sensitivity.

Figures 7a and 7b show all of the NO_2 adsorption mechanisms on the Cd and S sites of the CdS (111) surface. In the N-on-Cd configuration (Figure 7a), NO_2 interacts weakly with the surface through shallow coupling with Cd-5s states with indirect electron donation via Cd-S-3p surface hybrid orbitals [56]. This interaction has a small activation energy (E_a = 0.14 eV) and barely any charge transfer ($\Delta Q \approx +0.040$ e), resulting in little change of n-type conductivity through conduction-band interference. As a result, this pathway allows for a rapid but low-intensity sensing response controlled by weak physisorption. In comparison, the N-on-S system (Figure 7b) shows substantial orbital coupling between NO_2 frontier orbitals and surface S-3p states, showing direct electron donation via the lone pair on the S-3p orbitals [56]. This results in significant charge

transfer (ΔQ = +2.595 e) and greater adsorption energy (−0.88 eV), as well as considerable band-edge rehybridization, hole production, and partial shift towards p-type surface conductivity. The strong chemisorption property promotes high sensitivity and more stable sensing behavior, especially under extended exposure or high temperature conditions.

In this study, S-site adsorption dominates sensing performance through strong, direct electron donation via S-3p lone-pair orbitals, making it the main pathway governing effective NO_2 detection on CdS, while Cd-site adsorption supports fast but weak response due to indirect charge coupling (111). The strong S-site chemisorption and significant charge transfer correlate with the high experimental response observed at 125 °C, whereas the comparatively weaker Cd-site interaction explains the rapid response–recovery behavior due to lower activation barriers. Thus, the synergistic contribution of fast Cd-site activation and strong S-site chemisorption governs the overall NO_2 sensing performance of CdS QDs. In summary, Cd sites facilitate relatively weak but kinetically favorable adsorption, contributing to rapid response–recovery behavior, whereas S sites promote stronger chemisorption with significant charge transfer, governing the enhanced sensitivity and resistance modulation of the CdS QD sensor.

3.3 Experimental NO_2 detection study

The NO_2 sensing capabilities of the generated CdS QDs, including temperature response, selectivity analysis, concentration dependency, and response–recovery behavior, are summarized in Figure 8. Figure 8a illustrates how the sensor response for NO_2, NH_3, and H_2S varies with operation temperature. The mathematical description of the experimental sensing response (S) is

$$S\ (\%) = R_a - R_g/R_a \times 100 \tag{20}$$

Where, R_a is resistance in air, and R_g is resistance in gas atmosphere [57]. The response becomes extremely low at about 25 °C because there is not enough surface activation. In contrast to NH_3 and H_2S, which show much smaller response (48% and 32%), the response toward NO_2 increases significantly as the temperature rises over 75 °C and reaches a maximum of 72% at 125 °C.

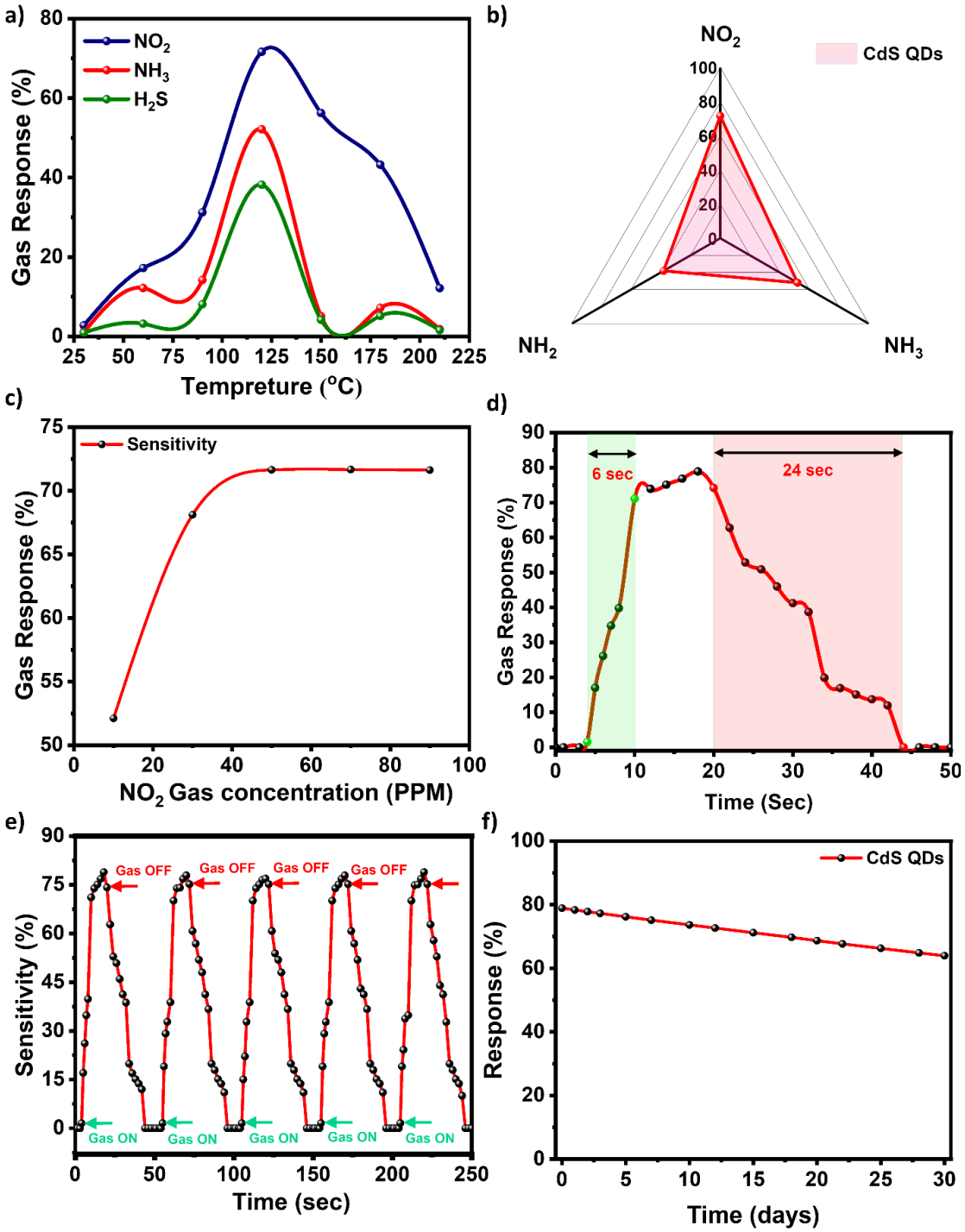

Figure 8. Gas detection study of as synthesized CdS QDs: a) Gas response analysis; b) Selectivity analysis of CdS QDs; c) Concentration effect on the NO_2 sensing performance of CdS QDs 125°C; d) Transient response and recovery times; e) Dynamic response recovery at a constant concentration (50 ppm); and f) Stability of the CdS QDs sensor at constant a concentration (50 ppm)

Its strong electron affinity, which facilitates effective electron removal from CdS QDs, is responsible for the improved NO_2 response. The reaction decreases at 125 °C because of increased thermal desorption, which shortens the gas–surface interaction time. The amazing selectivity of CdS QDs toward NO_2 is confirmed in Figure 8b, which shows a greater response in compared to NH_3 and H_2S. The stronger electron-acceptor nature of NO_2 is responsible for this selectivity, which is in line with the predictions of significant charge transfer at the S site. In ambient air, oxygen first adsorbs and generates O_2^-/O^- species by removing electrons from CdS. When subjected to NO_2, an extra electron is obtained via

$$NO_2\ (g)\ +\ e^-\ \rightarrow\ NO_2^- \qquad (21)$$

resulting in a substantial increase in resistance [58]. Conversely, reducing gases like NH_3 and H_2S donate electrons, leading to limited resistance modulation and hence lower sensing responses. The sensing response rises quickly from around 55% at 10 ppm NO_2 to about 70% at 40 ppm, then increases at about 72–73% above 70 ppm, as shown in Figure 8c. Strong gas affinity and quick adsorption kinetics are indicated by this quick rise, whereas saturation shows almost full occupancy of surface-active sites, which is in line with Langmuir adsorption behavior [59]. The quick response time (6 s) shown in Figure 8d indicates fast electron transfer via Cd sites, whereas stable chemisorption at S sites supports higher sensitivity at elevated concentration levels.

The structural and chemical stability of CdS QDs is confirmed by Figure 8f, which shows excellent long-term sensing stability with the response decreasing just slightly from 78% to 74% over 30 days. The Figure 8e shows switching cycles exhibit good repeatability and quick response (6 s) and recovery (24 s). Low-energy electron extraction is associated with the quick reaction, whereas recovery is driven by desorption and surface re-equilibration. Stable and reversible adsorption–desorption processes are confirmed by minimal hysteresis and minor drift, confirming CdS QDs as dependable options for high-performance NO_2 detection with superior sensitivity, fast response dynamics, and long-term operational stability.

As summarized in Table 3, the present CdS QD sensor demonstrates a comparatively higher NO_2 response (78% at 125 °C) than most previously reported sensing materials, particularly at moderate operating temperatures. The improved performance can be attributed to the quantum confinement–induced surface reactivity and the site-dependent adsorption mechanism that enables efficient

charge transfer and enhanced resistance modulation. These features collectively contribute to the superior sensitivity and rapid response behavior of the CdS QDs system.

Table 3. Comparative study of NO_2 gas sensing performance of CdS QDs with previously reported literature.

No.	Sensing Material	Response (%)	Target Gas	Temp (°C)	Reference
1	Rb-ZnO/In_2O_3	24.2 ($S = R_a/R_g$)	NO_2	100	[60]
2	SnS nanosheets	17.6 ($S = R_a/R_g$)	NO_2	150	[61]
3	ZnSe/ZnO	10.42 (S = Ra/Rg)	NO_2	200	[62]
4	MoS_2 NWs	18.1	NO_2	60	[64]
5	MoS_2 nanosphere/CTAB	60	NO_2	150	[63]
6	ZnO	1.04 and 36.17 ($S = R_a/R_g$)	NO_2	150	[65]
7	ZnO/CdO	10 to 22.6 ($S = R_a/R_g$)	NO_2	200	[66]
8	Ce/SnO_2	42.15 ($S = R_a/R_g$)	NO_2	140	[67]
9	SnO_2/rGO QDs	4.56 ($S = R_a/R_g$)	NO_2	200	[68]
10	**CdS QDs**	**78**	**NO_2**	**125**	**This study**

Conclusions

In this work, CdS QDs were successfully synthesized using a wet chemical method and deeply studied for NO_2 sensing using a combination of theoretical and experimental methods. The synthesis of exceptionally crystalline, quantum-confined CdS QDs with enhanced surface reactivity was verified by structural and optical characterizations. Strong NO_2 response (72% at

125 °C for 40 ppm), quick response (6 s) and recovery times (24 s), great selectivity over NH_3 and H_2S, and excellent long-term stability were all demonstrated for the sensor. DFT band-interaction analysis reveals that NO_2 adsorption on CdS is highly site-dependent due to differences in orbital alignment and charge-transfer pathways. At Cd sites, limited overlap between Cd-5s states and NO_2 frontier orbitals leads to weak electron transfer (+0.040 e) and shallow adsorption (−0.14 eV). In contrast, sulfur sites provide stronger N–S orbital hybridization and better energy matching, enabling direct electron donation from S-3p states. This results in significantly higher charge transfer (+2.595 e) and stronger chemisorption (−0.88 eV). The pronounced electronic redistribution at S sites induces substantial band modulation, explaining the enhanced NO_2 sensing performance. Rapid adsorption kinetics has been confirmed by characteristic time evaluation and theoretical sensing response, demonstrating the applicability of CdS QDs for real-time detection. While sensitivity is supported by higher charge localization at S sites, optical conductivity calculations further revealed increased carrier mobility for Cd-assisted contact. Together, the strong S-site chemisorption and fast Cd-site activation underpin the high sensitivity and rapid response of CdS QD sensors. In the end, CdS QDs are shown to be a promising material for selective, quick, and stable NO_2 sensing applications by the collaborative experimental–theoretical study.

ASSOCIATED CONTENT

Supporting Information

Additional data supporting this study are provided in the Supporting Information. This includes details of the gas sensing setup, morphological analysis (FESEM, EDS, and elemental mapping), and computational charge density difference maps for adsorption configurations. DFT-derived adsorption energy, Bader charge transfer, and electronic structure analyses (projected band structure, PDOS) are also presented. Optical property calculations of the CdS (111) surface and tabulated results for NO_2 adsorption configurations are included to further validate the experimental observations and correlate sensing response with theoretical insights.

Author Contributions

The manuscript was written through contributions of all authors. All authors have given approval to the final version of the manuscript.

Notes

The authors declare no competing financial interest.

Acknowledgment

KRZ and HMG acknowledge Deccan Education Society's Fergusson College (Autonomous) Pune for providing seed money support (30_9/2023-2024) for the research work. Authors also would like to acknowledge DST-FIST (Project No.: SR/FST/College-2011/090), Govt. of India for establishing laboratory facilities at college. Also, thanks to Savitribai Phule Pune University, Pune, for the characterization of samples. The authors would also like to thank the Centre for Development for Advanced Computing (CDAC) Pune for the computational facility.

References

[1]. Patil, S. V.; Kampara, R. K.; Venktesan, A.; Dongale, T. D.; Bae, J.; Devnath, A.; Seo, I.; Lee, S. Chemiresistive NO_2 Gas Sensor Based on RuO_2/MoS_2 Composite. J. Alloys Compd. 2025, 1036, 181748. https://doi.org/10.1016/j.jallcom.2025.181748

[2]. Xiao, H.-M.; Hou, Y.-C.; Guo, Y.-R.; Pan, Q.-J. The Coupling of Graphene, Graphitic Carbon Nitride and Cellulose to Fabricate Zinc Oxide-Based Sensors and Their Enhanced Activity towards Air Pollutant Nitrogen Dioxide. Chemosphere 2023, 324, 138325. https://doi.org/10.1016/j.chemosphere.2023.138325

[3]. Zhai, Y.; Yang, R.; Wu, J.; Li, J.; Xiang, K.; Hu, N.; Zeng, M.; Yang, J.; Yang, Z. Nitrogen Plasma-Driven Oxygen Vacancy Modulation in Tin Dioxide Nanosheets Enables Sub-Parts-per-Billion Nitrogen Dioxide Detection at Low Operating Temperature. ACS Sens. 2025, 10 (6), 4184–4193. https://doi.org/10.1021/acssensors.5c00298

[4]. Lou, C.; Wang, K.; Mei, H.; Xie, J.; Zheng, W.; Liu, X.; Zhang, J. ZnO Nanoarrays via a Thermal Decomposition–Deposition Method for Sensitive and Selective NO_2 Detection. CrystEngComm 2021, 23 (20), 3654–3663. https://doi.org/10.1039/d1ce00410g

[5]. Mane, A. T.; Kulkarni, S. B.; Navale, S. T.; Ghanwat, A. A.; Shinde, N. M.; Kim, J.; Patil, V. B. NO_2 Sensing Properties of Nanostructured Tungsten Oxide Thin Films. *Ceram. Int.* 2014, *40* (10), 16495–16502. https://doi.org/10.1016/j.ceramint.2014.08.001.

[6]. Mishra, A.; Basu, S.; Shetti, N. P.; Reddy, K. R. Metal Oxide Nanohybrids-Based Low-Temperature Sensors for NO_2 Detection: A Short Review. J. Mater. Sci.: Mater. Electron. 2019, 30 (9), 8160–8170. https://doi.org/10.1007/s10854-019-01232-0

[7]. Gandhi, M. Modelling Prospects of Bio-Electrochemical Immunosensing Platforms. Electrochem 2024, 5 (2), 146–161. https://doi.org/10.3390/electrochem5020010

[8]. Rigi Jangjoo, M.; Berahman, M. Room-Temperature Nitrogen Dioxide Gas Sensor Based on Graphene Oxide Nanoribbons Decorated with MoS_2 Nanospheres. Appl. Phys. A 2022, 128 (6). https://doi.org/10.1007/s00339-022-05605-x

[9]. Sakthivel, R.; Geetha, A.; Anandh, B. A.; Jagadeesan, V.; Ganesh, A. S.; Dineshkumar, J. Design of MoS_2/Graphene Heterostructure Thin Film Sensors for High-Performance NO_2 Gas Sensor Applications. J. Phys.: Conf. Ser. 2021, 2070 (1), 012131. https://doi.org/10.1088/1742-6596/2070/1/012131

[10]. Raza, A.; Hassan, J. Z.; Qumar, U.; Zaheer, A.; Babar, Z. U. D.; Iannotti, V.; Cassinese, A. Strategies for Robust Electrocatalytic Activity of 2D Materials: ORR, OER, HER, and CO_2RR. Mater. Today Adv. 2024, 22, 100488. https://doi.org/10.1016/j.mtadv.2024.100488

[11]. Chaudhary, P. L.; Adhyapak, P. V. Cadmium Sulfide Quantum Dots–Polythiophene Nanocomposite for Electrical Ammonia Sensing. J. Mater. Sci.: Mater. Electron. 2024, 35 (24). https://doi.org/10.1007/s10854-024-13394-7

[12]. Ebrahim, F.; Al-Hartomy, O.; Wageh, S. Cadmium-Based Quantum Dots Alloyed Structures: Synthesis, Properties, and Applications. Materials 2023, 16 (17), 5877. https://doi.org/10.3390/ma16175877

[13]. Feng, G.; Wang, S.; Wang, S.; Wang, P.; Wang, C.; Song, Y.; Xiao, J.; Song, C. Ultra-Sensitive Trace NO_2 Detection Based on Quantum Dots-Sensitized Few-Layer MXene: A Novel Convincing Insight into Dynamic Gas-Sensing Mechanism. Sens. Actuators, B 2024, 400, 134852. https://doi.org/10.1016/j.snb.2023.134852

[14]. Song, Z.-Y.; Li, Y.-Y.; Duan, W.; Xiao, X.-Y.; Gao, Z.-W.; Zhao, Y.-H.; Liang, B.; Chen, S.-H.; Li, P.-H.; Yang, M.; Huang, X.-J. Decisive Role of Electronic Structure in Electroanalysis for Sensing Materials: Insights from Density Functional Theory. TrAC, Trends Anal. Chem. 2023, 160, 116977. https://doi.org/10.1016/j.trac.2023.116977

[15]. Martínez-Castañón, G. Synthesis of CdS Nanoparticles: A Simple Method in Aqueous Media. Adv. Technol. Mater. Mater. Process. J. 2005, 7 (2), 171–174. https://doi.org/10.2240/azojomo0170

[16]. Giannozzi, P.; Baroni, S.; Bonini, N.; et al. QUANTUM ESPRESSO: A Modular and Open-Source Software Project for Quantum Simulations of Materials. J. Phys.: Condens. Matter 2009, 21 (39), 395502. https://doi.org/10.1088/0953-8984/21/39/395502

[17]. Giannozzi, P.; Andreussi, O.; Brumme, T.; et al. Advanced Capabilities for Materials Modelling with Quantum ESPRESSO. J. Phys.: Condens. Matter 2017, 29 (46), 465901. https://doi.org/10.1088/1361-648X/aa8f79

[18]. Vanderbilt, D. Soft Self-Consistent Pseudopotentials in a Generalized Eigenvalue Formalism. Phys. Rev. B 1990, 41, 7892–7895. https://doi.org/10.1103/PhysRevB.41.7892

[19]. Perdew, J. P.; Burke, K.; Ernzerhof, M. Generalized Gradient Approximation Made Simple. Phys. Rev. Lett. 1996, 77, 3865–3868. https://doi.org/10.1103/PhysRevLett.77.3865

[20]. Anisimov, V. I.; Zaanen, J.; Andersen, O. K. Band Theory and Mott Insulators: Hubbard U Instead of Stoner I. Phys. Rev. B 1991, 44 (3), 943. https://doi.org/10.1103/PhysRevB.44.943

[21]. Monkhorst, H. J.; Pack, J. D. Special Points for Brillouin-Zone Integrations. *Phys. Rev. B* 1976, *13*, 5188. https://doi.org/10.1103/PhysRevB.13.5188

[22]. van Setten, M. J.; Giantomassi, M.; Bousquet, E.; et al. The PseudoDojo: Training and Grading an 85 Element Optimized Norm-Conserving Pseudopotential Table. *Comput. Phys. Commun.* 2018, *226*, 39–54. https://doi.org/10.1016/j.cpc.2018.01.012

[23]. Benassi, A.; Ferretti, A.; Cavazzoni, C. *PWSCF's epsilon.x User's Manual*; Università degli Studi di Modena e Reggio Emilia, INFM/S3, and CINECA Consorzio Interuniversitario: Online Manual. https://web.mit.edu/espresso_v6.1/amd64_ubuntu1404/qe-6.1/PP/Doc/eps_man.pdf

[24]. Biswas, A.; Ghosh, S.; Saha, S.; Saha, S. Electronic and Band Structure Calculation of CdS Using GGA and GGA+U Functionals. *J. Phys.: Conf. Ser.* 2022, *2267*, 012155. https://doi.org/10.1088/1742-6596/2267/1/012155

[25]. Khan, M. J. I.; Kanwal, Z.; Yousaf, M.; et al. Investigating Structural, Electronic and Optical Properties of CdS:Cr (A GGA and GGA+U Study). *Solid State Sci.* 2020, *108*, 106437. https://doi.org/10.1016/j.solidstatesciences.2020.106437

[26]. Henkelman, G.; Arnaldsson, A.; Jónsson, H. A Fast and Robust Algorithm for Bader Decomposition of Charge Density. *Comput. Mater. Sci.* 2006, *36* (3), 354–360. https://doi.org/10.1016/j.commatsci.2005.04.010

[27]. Xiong, S.; Isaacs, E. B.; Li, Y. Adsorption Characteristics and Size/Shape Dependence of Pt Clusters on the CdS Surface. *J. Phys. Chem. C* 2015, *119* (9), 4834–4842. https://doi.org/10.1021/jp5117646

[28]. Chhana, L.; Lalroliana, B.; Tiwari, R. C.; et al. Theoretical Study of ZnS Monolayer Adsorption Behavior for CO and HF Gas Molecules. *ACS Omega* 2022, *7* (44), 40176–40183. https://doi.org/10.1021/acsomega.2c05064

[29]. Henkelman, G.; Uberuaga, B. P.; Jónsson, H. A climbing image nudged elastic band method for finding saddle points and minimum energy paths. J. Chem. Phys. 2000, 113, 9901−9904. https://doi.org/10.1063/1.1329672

[30]. Li, K.; Luo, Y.; Liu, B.; Gao, L.; Duan, G. High-Performance NO_2-Gas Sensing of Ultrasmall $ZnFe_2O_4$ Nanoparticles Based on Surface Charge Transfer. *J. Mater. Chem. A* 2019, *7* (10), 5539–5551. https://doi.org/10.1039/C8TA12168K

[31]. Giri, R. K.; Chaki, S. H.; Dave, M. S.; *et al. First principle insights and experimental investigations of the electronic and optical properties of* $CuInS_2$ *single crystals.* Mater. Adv. 2023, *4*(15), 3246–3256. https://doi.org/10.1039/d3ma01234a

[32]. Kuzmenko, A. B. *Kramers–Kronig constrained variational analysis of optical spectra.* Rev. Sci. Instrum. 2005, *76*, 083108. https://doi.org/10.1063/1.1979470

[33]. Tarekuzzaman, M.; Ishraq, M. H.; Shahadath, N.; *et al. DFT analysis of structural, electronic, optical, and thermodynamic properties of* $LiXI_3$ *(where X = Ca, Sr, Ba) halide perovskites for optoelectronics.* Sci. Rep. 2025, *15*, 25304. https://doi.org/10.1038/s41598-025-91458-2

[34]. Tangirbergen, A.; Yergaliuly, G.; Wang, Y.; Tsoukalas, L.; Mentbayeva, A.; Soltabayev, B. *Multiscale design of metal oxide semiconductor gas sensors: A DFT-driven perspective on structure–property–function relationships.* Mater. Des. 2025, *258*, 114647. https://doi.org/10.1016/j.matdes.2025.114647

[35]. Rao, B. S.; Kumar, B. R.; Reddy, V. R.; Rao, T. S.; Chalapathi, G. J. *Preparation and characterization of CdS nanoparticles by chemical co-precipitation technique.* Chalcogenide Lett. 2011, *8*(3), 177–185. https://doi.org/10.1201/b18247-14.

[36]. Basak, M.; Rahman, M. L.; Ahmed, M. F.; Biswas, B.; Sharmin, N. *The use of X-ray diffraction peak profile analysis to determine the structural parameters of cobalt ferrite nanoparticles using Debye–Scherrer, Williamson–Hall, Halder–Wagner and size–strain plot: Different precipitating agent approach.* J. Alloys Compd. 2022, *895*, 162694. https://doi.org/10.1016/j.jallcom.2021.162694

[37]. Singh, V.; Chauhan, P. *Structural and optical characterization of CdS nanoparticles prepared by chemical precipitation method.* J. Phys. Chem. Solids 2009, *70*(7), 1074–1079. https://doi.org/10.1016/j.jpcs.2009.05.024

[38]. Klein, J.; Kampermann, L.; Mockenhaupt, B.; Behrens, M.; Strunk, J.; Bacher, G. *Limitations of the Tauc plot method.* Adv. Funct. Mater. 2023, *33*(47), 2304523. https://doi.org/10.1002/adfm.202304523

[39]. Lee, H.; Issam, A.; Belmahi, M.; Assouar, M.; Rinnert, H.; Alnot, M. *Synthesis and characterizations of bare CdS nanocrystals using chemical precipitation method for photoluminescence application.* J. Nanomater. 2009, *2009*, 1–9. https://doi.org/10.1155/2009/914501

[40]. Narayanan, S. S.; Pal, S. K. *Aggregated CdS quantum dots: host of biomolecular ligands.* J. Phys. Chem. B 2006, *110*(48), 24403–24409. https://doi.org/10.1021/jp064180w

[41]. Singh, N.; Mehra, R.; Kapoor, A.; Soga, T. *ZnO based quantum dot sensitized solar cell using CdS quantum dots.* J. Renewable Sustainable Energy 2012, *4*(1). https://doi.org/10.1063/1.3683531

[42]. Zhao, H.; Sirigu, G.; Parisini, A.; Camellini, A.; Nicotra, G.; Rosei, F.; Morandi, V.; Zavelani-Rossi, M.; Vomiero, A. *Nanoscale* **2016**, *8*, 4217–4226. https://doi.org/10.1039/c5nr08881j

[43]. Du, H.; Liang, K.; Yuan, C.-Z.; *et al. Bare* Cd_{1}*–x*Zn_{x}*S ZB/WZ heterophase nanojunctions for visible light photocatalytic hydrogen production with high efficiency.* ACS Appl. Mater. Interfaces 2016, *8*(37), 24550–24558. https://doi.org/10.1021/acsami.6b06182

[44]. Singh, V.; Sharma, P. K.; Chauhan, P. *Synthesis of CdS nanoparticles with enhanced optical properties.* Mater. Charact. 2011, *62*, 43–52. https://doi.org/10.1016/j.matchar.2010.10.009

[45]. Cao, Y.; Hu, P.; Jia, D. *Phase- and shape-controlled hydrothermal synthesis of CdS nanoparticles, and oriented attachment growth of its hierarchical architectures.* Appl. Surf. Sci. 2013, *265*, 771–777. https://doi.org/10.1016/j.apsusc.2012.11.107

[46]. Pan, J.; Liu, J.; Ma, H.; *et al. Structure of flower-like hierarchical CdS QDs/Bi/Bi_2WO_6 heterojunction with enhanced photocatalytic activity.* New J. Chem. 2018, *42*(9), 7293–7300. https://doi.org/10.1039/C8NJ00394G

[47]. Singh, K. J.; Ahmed, T.; Gautam, P.; *et al. Recent advances in two-dimensional quantum dots and their applications.* Nanomaterials 2021, *11*(6), 1549. https://doi.org/10.3390/nano11061549

[48]. Zhang, N.; Liu, X.; Wei, Z.; *et al. Cell imaging using two-photon excited CdS fluorescent quantum dots working within the biological window.* Nanomaterials 2019, *9*, 369. https://doi.org/10.3390/nano9030369

[49]. Bala, M.; Rahman, M. T.; Nahean, R.; Hasan Khan, M. *NO_2 and SO_2 adsorption and sensing on Janus B_2SeTe: unveiling its electronic, optical, and magnetic properties through DFT and COMSOL.* RSC Adv. 2025, *15*, 25187–25201. https://doi.org/10.1039/D5RA04190B

[50]. Park, S.; Siahrostami, S.; Park, J.; *et al. Effect of adventitious carbon on pit formation of monolayer MoS_2.* Adv. Mater. 2020, *32*, 2003020. https://advanced.onlinelibrary.wiley.com/journal/15214095

[51]. Lin, L.; Li, X.; Xue, C.; Cai, X.; Tao, H.; Zhang, Z. $MoSe_2$ Crystalline Nanosheets for Room-Temperature Ammonia Sensing, Langmuir 2023, *39*(42), 15142–15151. https://doi.org/10.1021/acs.langmuir.3c02464

[52]. Kushwaha, A.; Goel, N. *A DFT study of superior adsorbate–surface bonding at Pt–WSe_2 vertically aligned heterostructures upon NO_2, SO_2, CO_2, and H_2 interactions.* Sci. Rep. 2024, *14*, 15708. https://doi.org/10.1038/s41598-024-65213-y

[53]. Cui, H.; Jia, P.; Peng, X.; Hu, X. Geometric, Electronic and Optical Properties of Pt-Doped C_3N Monolayer upon NO_x Adsorption: A DFT Study. *IEEE Sens. J.* 2020, *PP*, 1–1. https://doi.org/10.1109/JSEN.2020.3028138

[54]. Hussein, T.; Shiltagh, N.; Alaarage, W.; Abbas, R.; Jawad, R.; Kadhim, A. A.; Abo Nasria, A. H. Electronic and Optical Properties of the BN Bilayer as Gas Sensor for CO_2, SO_2, and NO_2 Molecules: A DFT Study. *Results Chem.* 2023, *5*, 100978. https://doi.org/10.1016/j.rechem.2023.100978

[55]. Aldaghfag, S.; Yaseen, M.; Ambreen, H.; Butt, M.; Rehan, M.; Dahshan, A. Effect of Fe on Physical Characteristics of CdS: DFT Investigations. *Chalcogenide Lett.* **2021**, *18*, 357–365. https://doi.org/10.15251/CL.2021.187.357

[56]. Xu, C.; Tu, J.; Qiu, H.; Liao, N. *First principles investigation of sensing mechanism of CdS monolayer for detecting NO_2 from H_2S, CO_2, NH_3, CO, CH_4 gases.* Phys. Lett. A 2025, *564*, 131102. https://doi.org/10.1016/j.physleta.2025.131102

[57]. Kadam, S. S.; Mandawade, A. S.; Zoting, K. R.; *et al. Biofabrication of CeO_2 nanostructure using Bryophyllum pinnatum leaf extract for CO gas detection and DFT studies.* Ionics 2025, *31*, 9935–9952. https://doi.org/10.1007/s11581-025-06524-6

[58]. Patil, Vikas ; Navale, Sachin ; Chougule, Manik ; Shinde, Nanasaheb .M. ; Kim, Junho.. Highly Selective and Sensitive CdS Thin Film Sensor for Detection of NO2 Gas. RSC Adv.. 4. (2014) https://doi.org/10.1039/C4RA06531J.

[59]. Latour, R. A. The Langmuir Isotherm: A Commonly Applied but Misleading Approach for the Analysis of Protein Adsorption Behavior. *J. Biomed. Mater. Res., Part A* 2015, *103* (3), 949–958. https://doi.org/10.1002/jbm.a.35235

[60]. Yang, Y.; Cui, J.; Luo, Z.; Luo, Z.; Sun, Y. *Enhanced NO_2 gas sensing properties based on Rb-doped ZnO/In_2O_3 heterojunctions at room temperature: A combined DFT and experimental study.* Sensors 2024, *24*(16), 5311. https://doi.org/10.3390/s24165311

[61]. Pengtao Wang, Wanyin Ge, Long Lin, Xiaohua Jia, Xinmeng Zhang, Jing Lu, Ultra-sensitive NO2 detection based on SnS nanosheets: Experimental and DFT investigation, Vacuum, Volume 209, 2023, 111777, ISSN 0042-207X, https://doi.org/10.1016/j.vacuum.2022.111777.

[62]. Liu, W.; Gu, D.; Li, X. *Ultrasensitive NO_2 detection utilizing mesoporous ZnSe/ZnO heterojunction-based chemiresistive-type sensors.* ACS Appl. Mater. Interfaces 2019, *11*(32), 29029–29040. https://doi.org/10.1021/acsami.9b07263

[63]. Zhang, Y.; Zeng, W.; Li, Y. Hydrothermal Synthesis and Controlled Growth of Hierarchical 3D Flower-like MoS_2 Nanospheres Assisted with CTAB and Their NO_2 Gas Sensing Properties. *Appl. Surf. Sci.* 2018, *455*, 276–282. https://doi.org/10.1016/j.apsusc.2018.05.224

[64]. Kumar, R.; Goel, N.; Kumar, M. High-Performance NO_2 Sensor Using MoS_2 Nanowires Network. *Appl. Phys. Lett.* 2018, *112* (5), 053502. https://doi.org/10.1063/1.5019296

[65]. Sun, N.; et al. Highly Sensitive and Lower Detection-Limit NO_2 Gas Sensor Based on Rh-Doped ZnO Nanofibers Prepared by Electrospinning. *Appl. Surf. Sci.* 2023, *614*, 156213. https://doi.org/10.1016/j.apsusc.2022.156213

[66]. Naderi, H.; Hajati, S.; Ghaedi, M.; Espinos, J. Highly Selective Few-ppm NO Gas Sensing Based on Necklace-like Nanofibers of ZnO/CdO n–n Type I Heterojunction. *Sens. Actuators, B* 2019, *297*, 126774. https://doi.org/10.1016/j.snb.2019.126774

[67]. Liu, H.; Liu, B.; Li, P.; Kang, W.; Zhang, Y. High Sensitivity and Anti-Humidity Gas Sensor for Nitrogen Dioxide Based on Ce/SnO_2 Nanomaterials. *Sens. Actuators, A* 2022, *344*, 113717. https://doi.org/10.1016/j.sna.2022.113717

[68]. Bhangare, B.; Ramgir, N. S.; Jagtap, S.; et al. XPS and Kelvin Probe Studies of SnO_2/RGO Nanohybrids-Based NO_2 Sensors. *Appl. Surf. Sci.* 2019, *487*, 918–929. https://doi.org/10.1016/j.apsusc.2019.05.176